

1
2
3
4
5
6
7
8
9
10
11
12
13
14
15
16
17
18
19
20

**Constraining the strength of the terrestrial CO₂ fertilization
effect in the Canadian Earth System Model version 4.2
(CanESM4.2)**

V. K. Arora and J. F. Scinocca.

Canadian Centre for Climate Modelling and Analysis, Environment and Climate Change Canada,
University of Victoria, Victoria, B.C., V8W 2Y2, Canada

21 **Abstract**

22

23 Earth system models (ESMs) explicitly simulate the interactions between the physical climate
24 system components and biogeochemical cycles. Physical and biogeochemical aspects of ESMs
25 are routinely compared against their observation-based counterparts to assess model performance
26 and to evaluate how this performance is affected by ongoing model development. Here, we assess
27 the performance of version 4.2 of the Canadian Earth system model against four, land carbon
28 cycle focused, observation-based determinants of the global carbon cycle and the historical global
29 carbon budget over the 1850-2005 period. Our objective is to constrain the strength of the
30 terrestrial CO₂ fertilization effect which is known to be the most uncertain of all carbon cycle
31 feedbacks. The observation-based determinants include 1) globally-averaged atmospheric CO₂
32 concentration, 2) cumulative atmosphere-land CO₂ flux, 3) atmosphere-land CO₂ flux for the
33 decades of 1960s, 1970s, 1980s, 1990s and 2000s and 4) the amplitude of the globally-averaged
34 annual CO₂ cycle and its increase over the 1980 to 2005 period. The optimal simulation that
35 satisfies constraints imposed by the first three determinants yields a net primary productivity
36 (NPP) increase from ~58 Pg C/yr in 1850 to about ~74 Pg C/yr in 2005; an increase of ~27% over
37 the 1850-2005 period. The simulated loss in the global soil carbon amount due to anthropogenic
38 land use change over the historical period is also broadly consistent with empirical estimates. Yet,
39 it remains possible that these determinants of the global carbon cycle are insufficient to
40 adequately constrain the historical carbon budget, and consequently the strength of terrestrial CO₂
41 fertilization effect as it is represented in the model, given the large uncertainty associated with
42 LUC emissions over the historical period.

43

44 **1. Introduction**

45

46 The evolution of the atmospheric CO₂ concentration in response to anthropogenic fossil fuel CO₂
47 emissions is determined by the rate at which a fraction of these emissions is taken up by the land
48 and ocean. Had the land and ocean not provided this “ecosystem service” since the start of the
49 industrial era, and not removed about 50% of CO₂ emissions from the atmosphere (Knorr, 2009),
50 the present concentration of CO₂ in the atmosphere would have been around 500 ppm, compared
51 to its current value of around 400 ppm. Over land, temperate and boreal forests as well as forests
52 in the tropical region are known to be sinks of atmospheric carbon (Ciais et al., 2013; Gourdji et
53 al., 2012; Schimel et al., 2015). The sink in the tropical forests is, however, compensated by
54 anthropogenic land use change emissions (Phillips and Lewis, 2014). Over ocean, the uptake of
55 anthropogenic carbon is observed to be larger in the high latitudes than in the tropical and
56 subtropical regions (Khatiwala et al., 2009). The manner in which the land and ocean will
57 continue to provide this ecosystem service in future is of both scientific and policy relevance.

58

59 Future projections of atmospheric CO₂ concentration, [CO₂], in response to continued
60 anthropogenic CO₂ emissions, or alternatively projections of CO₂ emissions compatible with a
61 given future [CO₂] pathway, are based primarily on comprehensive Earth system models (ESMs)
62 which include interactive land and ocean carbon cycle components (Jones et al., 2013). The land
63 and ocean carbon cycle components in ESMs respond both to increases in [CO₂] as well as the
64 associated changes in climate. These carbon components also respond to changes in climate
65 associated with other forcings including changes in concentration of non-CO₂ greenhouse gases
66 and aerosols, to nitrogen deposition and over land to anthropogenic land use change (LUC).

67

68 The response of land and ocean carbon cycle components to changes in [CO₂] and the associated
69 change in climate is most simply characterized in the framework of the 140-year long 1% per year
70 increasing CO₂ (1pctCO₂) experiment, in which [CO₂] increases at a rate of 1% per year from
71 pre-industrial value of about 285 ppm until concentration quadruples to about 1140 ppm. The
72 1pctCO₂ experiment has been recognized as a standard experiment by the coupled model
73 intercomparison project (CMIP) which serves to quantify the response of several climate and
74 Earth system metrics to increasing CO₂. These metrics include the transient climate response
75 (TCR) and the transient climate response to cumulative emissions (TCRE, Gillett et al., 2013).
76 Arora et al. (2013) analyzed results from fully-, biogeochemically- and radiatively-coupled
77 versions of the 1pctCO₂ experiment from eight ESMs that participated in the phase five of the
78 CMIP (CMIP5). They calculated the response of land and ocean carbon cycle components to
79 changes in [CO₂] and the associated change in climate expressed in terms of carbon-concentration
80 and carbon-climate feedbacks, respectively. Arora et al. (2013) found that of all the carbon cycle
81 feedbacks, the carbon-concentration feedback over land, which is primarily determined by the
82 strength of the terrestrial CO₂ fertilization effect, is the most uncertain across models. They found
83 that while the uncertainty in the carbon-concentration feedback over land (expressed in terms of
84 the standard deviation of the magnitude of the feedbacks) had somewhat reduced since the first
85 coupled carbon cycle climate model intercomparison project (C⁴MIP) (Friedlingstein et al., 2006)
86 its uncertainty remained the largest of all carbon cycle feedbacks. The comparison of the actual
87 magnitudes of the carbon cycle feedbacks over land is, however, not straightforward between the
88 Arora et al. (2013) and Friedlingstein et al. (2006) studies because they used different CO₂
89 scenarios.

90

91 The reason for this large uncertainty is that it is fairly difficult at present to constrain the strength
92 of the terrestrial CO₂ fertilization effect at the global scale. The net atmosphere-land CO₂ flux
93 since the start of the industrial era has not only been influenced by the changes in [CO₂] but also
94 the associated change in climate (due both to changes in [CO₂] and other climate forcings),
95 nitrogen deposition, and more importantly land use change - the contribution of which itself
96 remains highly uncertain. Since it is difficult to estimate the observed magnitude of net
97 atmosphere-land CO₂ flux since the start of the industrial era attributable only to increase in
98 [CO₂] it is consequently difficult to estimate the strength of the terrestrial CO₂ fertilization effect.

99
100 Measurements at Free-Air CO₂ Enrichment (FACE) sites in which vegetation is exposed to
101 elevated levels of [CO₂] help to assess some aspects of CO₂ fertilization and how nutrients
102 constraints regulate photosynthesis at elevated [CO₂] (Medlyn et al., 1999; McGuire et al., 1995).
103 However, FACE results cannot be easily extrapolated to the global scale and the response of
104 vegetation corresponds to a step increase in [CO₂] not the gradual increase which the real world
105 vegetation is experiencing.

106
107 As part of the ongoing evaluation of carbon cycle in ESMs, the model simulated aspects of the
108 global carbon cycle are routinely evaluated against their observation-based counterparts. These
109 evaluations also provide the opportunity to adjust physical processes that influence the strength of
110 the terrestrial CO₂ fertilization effect to provide the best comparison with observation-based
111 aspects of the global carbon cycle. Here, we present results from such an evaluation for a new
112 version of the Canadian Earth system model (CanESM4.2). An earlier version of the Canadian
113 Earth system model (CanESM2, Arora et al., 2011) participated in the CMIP5 (Taylor et al. 2012)

114 and its results also contributed to the fifth assessment report (AR5) of the Intergovernmental
115 Panel on Climate Change (IPCC). We evaluate the response of CanESM4.2, for three different
116 strengths of the terrestrial CO₂ fertilization effect, against four observation-based determinants of
117 the global carbon cycle and the historical global carbon budget over the 1850-2005 period, with a
118 focus on the land carbon cycle component. These determinants include 1) globally-averaged
119 atmospheric CO₂ concentration, 2) cumulative atmosphere-land CO₂ flux, 3) atmosphere-land
120 CO₂ flux for the decades of 1960s, 1970s, 1980s, 1990s and 2000s, and 4) the amplitude of the
121 globally-averaged annual CO₂ cycle and its increase over the 1980 to 2005 period.

122
123 The strength of the CO₂ fertilization effect influences all four of these determinants of the global
124 carbon cycle and the historical carbon budget. A stronger CO₂ fertilization effect, of course,
125 implies a larger carbon uptake by land and consequently a lower rate of increase of [CO₂] in
126 response to anthropogenic fossil fuel emissions. However, the strength of the CO₂ fertilization
127 effect also influences the amplitude of the annual [CO₂] cycle which is primarily controlled by the
128 northern hemisphere's biospheric activity. The amplitude of the annual [CO₂] cycle has been
129 observed to increase over the past five decades suggesting a gradual increase in photosynthesis in
130 association with a strengthening of the CO₂ fertilization effect (Keeling et al., 1996 ; Randerson et
131 al., 1997) and thus possibly can help to constrain the strength of the terrestrial CO₂ fertilization
132 effect in Earth system models.

133

134 **2. The coupled climate-carbon system and CanESM4.2**

135

136 **2.1 The coupled climate-carbon system**

137

138 The globally-averaged and vertically-integrated carbon budget for the combined atmosphere-
 139 land-ocean system may be written as:

$$140 \frac{dH_G}{dt} = \frac{dH_A}{dt} + \frac{dH_L}{dt} + \frac{dH_O}{dt} = E_F \quad (1)$$

142 where the Global carbon pool $H_G = H_A + H_L + H_O$ is the sum of carbon in the Atmosphere, Land
 144 and Ocean components, respectively (Pg C), and E_F is the rate of anthropogenic CO₂ emissions
 145 (Pg C/yr) into the atmosphere. The equations for the atmosphere, land and ocean components are
 146 written as

$$147 \begin{aligned} \frac{dH_A}{dt} &= F_A + E_F \\ &= -F_L - F_O + E_F \\ &= -(F_l - E_L) - F_O + E_F \\ &= -F_l - F_O + E_F + E_L \end{aligned} \quad (2)$$

$$\frac{dH_L}{dt} = F_L = F_l - E_L$$

$$\frac{dH_O}{dt} = F_O$$

149 where $(F_L + F_O) = -F_A$ are the fluxes (Pg C/yr) between the atmosphere and the underlying land
 151 and ocean, taken to be positive into the components. The net atmosphere-land CO₂ flux
 152 $F_L = F_l - E_L$ is composed of LUC emission rate E_L (Pg C/yr) as well as the remaining global
 153 “natural” CO₂ flux F_l that is often referred to as the residual or missing land sink in the context of
 154 the historical carbon budget (Le Quéré et al., 2015). The emissions associated with LUC occur
 155 when natural vegetation, for example, is deforested and replaced by croplands resulting in net loss
 156 of carbon from land to the atmosphere (i.e. positive E_L). Conversely, when croplands are

157 abandoned and gradually replaced by forests then carbon is gained from atmosphere into the land
 158 (i.e. negative E_L).

159
 160 Over land, the rate of change of carbon is reflected in the model's three land pools (vegetation, V ;
 161 soil, S ; and litter or detritus, D)

$$\begin{aligned}
 \frac{dH_L}{dt} &= F_L = F_l - E_L \\
 &= \frac{dH_V}{dt} + \frac{dH_S}{dt} + \frac{dH_D}{dt} \\
 &= (G - R_A) - R_H - E_L \\
 &= N - R_H - E_L
 \end{aligned} \tag{3}$$

163 where G is the gross primary productivity (Pg C/yr) which represents the rate of carbon uptake by
 164 vegetation through photosynthesis, and R_A and R_H are the autotrophic and heterotrophic
 165 respiratory fluxes (Pg C/yr) from living vegetation and dead litter and soil carbon pools,
 166 respectively. $N = G - R_A$ is the net primary productivity (NPP) which represents the carbon
 167 uptake by vegetation after autotrophic respiratory costs have been taken into account. The
 168 heterotrophic respiration $R_H = R_{H,D} + R_{H,S}$ is composed of respiration from the litter and soil
 169 carbon pools. The rate of change in carbon in model's litter (H_D) and soil (H_S) pools is written as

$$\begin{aligned}
 \frac{dH_D}{dt} &= D_L + D_S + D_R - C_{D \rightarrow S} - R_{H,D} \\
 \frac{dH_S}{dt} &= C_{D \rightarrow S} - R_{H,S}
 \end{aligned} \tag{4}$$

171 where $D_{i,i=L,S,R}$ is the litter fall from the model's Leaf, Stem and Root components into the
 172 model's litter pool. $C_{D \rightarrow S}$ is the transfer of humidified litter into the soil carbon pool calculated as
 173 a fraction of the litter respiration ($R_{H,D}$)

$$C_{D \rightarrow S} = \chi R_{H,D} \tag{5}$$

175 and χ is the humification factor.

176

177 Integrating (2) and (3) in time with $\int_{t_0}^t (dH/dt)dt = H(t) - H(t_0) = \Delta H(t)$ and $\int_{t_0}^t F dt = \tilde{F}(t)$ (Pg

178 C) gives

$$\begin{aligned}\Delta H_A &= -(\tilde{F}_O + \tilde{F}_l) + (\tilde{E}_F + \tilde{E}_L) \\ \Delta H_O &= \tilde{F}_O \\ \Delta H_L &= \tilde{F}_L = \tilde{F}_l - \tilde{E}_L; \\ &= \Delta H_V + \Delta H_S + \Delta H_D = \tilde{F}_l - \tilde{E}_L = \tilde{N} - \tilde{R}_H - \tilde{E}_L \\ \Delta H_l &= \tilde{F}_l \\ \Delta H &= \tilde{E}_F\end{aligned}\tag{6}$$

180 The cumulative change in the atmosphere, the ocean and the land carbon pools is written as

$$\begin{aligned}\Delta H_A + \Delta H_O + (\Delta H_l - \tilde{E}_L) &= \tilde{E}_F \\ \Delta H_A + \Delta H_O + \Delta H_l &= \tilde{E}_F + \tilde{E}_L = \tilde{E}\end{aligned}\tag{7}$$

182 where \tilde{E} (Pg C) is the cumulative sum of the anthropogenic emissions from fossil fuel
183 consumption and land use change. When emissions associated with LUC are zero, equation (7)
184 becomes

$$\Delta H_A + \Delta H_O + \Delta H_L = \tilde{E}_F = \tilde{E}\tag{8}$$

186 which indicates how cumulative emissions are parsed into changes in atmospheric carbon burden
187 and carbon uptake by the ocean and land components.

188

189 **2.2 Canadian Earth System Model version 4.2**

190

191 **2.2.1 Physical components**

192
193 At the Canadian Centre for Climate Modelling and Analysis (CCCma), the earth system model,
194 CanESM2, has undergone further development since its use for CMIP5. This version of the
195 model has been equivalently labelled CanESM4.0 in an effort to rationalize the ESM naming
196 convention to better reflect the fact that this model version employs the 4th generation atmosphere
197 component, CanAM4, (Von Salzen et al. 2013) and the 4th generation ocean component, CanOM4
198 (Arora et al., 2011). The version of the CCCma earth system model used for this study is
199 CanESM4.2 and so, represents two full cycles of model development on all of its components.
200 Similar to CanESM2, the physical ocean component of CanESM4.2 (CanOM4.2) has 40 levels
201 with approximately 10 m resolution in the upper ocean while the horizontal ocean resolution is
202 approximately 1.41° (longitude) \times 0.94° (latitude). The majority of development in CanESM4.2,
203 relative to CanESM2, has occurred on its atmospheric component CanAM4.2. CanAM4.2 is a
204 spectral model employing T63 triangular truncation with physical tendencies calculated on a 128
205 \times 64 ($\sim 2.81^\circ$) horizontal linear grid with 49 layers in the vertical whose thicknesses increase
206 monotonically with height to 1 hPa. Relative to CanAM4, CanAM4.2 includes a new version of
207 the Canadian Land Surface Scheme, CLASS3.6, which models the energy and water fluxes at the
208 atmosphere-land boundary by tracking energy and water through the soil, snow, and vegetation
209 canopy components (Verseghy, 2012). CLASS models the land surface energy and water balance
210 and calculates liquid and frozen soil moisture, and soil temperature for three soil layers (with
211 thicknesses 0.1, 0.25 and 3.75 m). The thickness of the third layer depends on the depth to
212 bedrock (and is in many places less than 3.75 m) based on the Zabler (1986) soil data set.
213 Changes to CLASS primarily include improvements to the simulation of snow at the land surface.
214 These incorporate new formulations for vegetation interception of snow (Bartlett et al., 2006), for

215 unloading of snow from vegetation (Hedstrom and Pomeroy, 1998), for the albedo of snow-
216 covered canopies (Bartlett and Verseghy, 2015), for limiting snow density as a function of depth
217 (Tabler et al., 1990; Brown et al., 2006), and for the thermal conductivity of snow (Sturm et al.,
218 1997). Water retention in snowpacks has also been incorporated. CanAM4.2 also includes an
219 aerosol microphysics scheme (von Salzen, 2006; Ma et al., 2008; Peng et al., 2012), a higher
220 vertical resolution in the upper troposphere, a reduced solar constant (1361W/m^2) and an
221 improved treatment of the solar continuum used in the radiative transfer. CanAM4.2 also
222 considers natural and anthropogenic aerosols and their emissions, transport, gas-phase and
223 aqueous-phase chemistry, and dry and wet deposition as summarized in Namazi et al. (2015)

224

225 **2.2.2 Land and ocean carbon cycle components**

226

227 The ocean and land carbon cycle components of CanESM4.2, are similar to CanESM2, and
228 represented by the Canadian Model of Ocean Carbon (CMOC) (Christian et al., 2010) and the
229 Canadian Terrestrial Ecosystem Model (CTEM) (Arora et al., 2009; Arora and Boer, 2010),
230 respectively.

231

232 LUC emissions in CTEM are modelled interactively on the basis of changes in land cover which
233 are determined by changes in crop area. The historical land cover used in the simulations
234 presented here is reconstructed using the linear approach of Arora and Boer (2010) and is the
235 same as used for CMIP5 simulations; as the fraction of crop area in a grid cell changes, the
236 fraction of non-crop plant functional types (PFTs) is adjusted linearly in proportion to their
237 existing coverage. The historical changes in crop area are based on the data set provided for

238 CMIP5 simulations as explained in Arora and Boer (2014). When the fraction of crop area in a
 239 grid cell increases then the fractional coverage of other PFTs is reduced which results in
 240 deforested biomass. The deforested biomass is allocated to three components that are i) burned
 241 instantaneously and contribute to ii) short (paper) and iii) long (wood products) term pools (Arora
 242 and Boer, 2010). The deforested biomass corresponding to paper and wood products is
 243 transferred to model's litter and soil carbon pools, respectively. When the fraction of crop area
 244 decreases, the fractional coverage of non-crop PFTs increases and their vegetation biomass is
 245 spread over a larger area reducing vegetation density. Carbon is sequestered until a new
 246 equilibrium is reached providing a carbon sink associated with regrowth as the abandoned areas
 247 revert back to natural vegetation.

248
 249 The LUC emissions term (E_L) in the equations (1) through (8) is not easily defined or calculated.
 250 Pongratz et al. (2014) discuss the multiple definitions and methods of calculating E_L . When E_L
 251 is calculated using models, it is most usually defined as the difference in F_L between simulations
 252 with and without LUC. This is also the basic definition used by Pongratz et al. (2014).
 253 Calculating E_L thus requires performing additional simulations without land use change in which
 254 land cover is held constant at its pre-industrial state. For a simulation without LUC equation (3)
 255 becomes

$$256 \quad \frac{dH'_L}{dt} = F'_L = F'_l \quad (9)$$

257 and an estimate of E_L , and its cumulative values \tilde{E}_L , is obtained as

$$258 \quad \begin{aligned} E_L &= F'_L - F_L \\ \tilde{E}_L &= \tilde{F}'_L - \tilde{F}_L \end{aligned} \quad (10)$$

259 Over the historical period, globally, F'_L is expected to be higher than F_L (both considered
260 positive downwards) due, at least, to two processes: 1) fraction of deforested biomass that is
261 burned and which contributes to short and long term product pools all release carbon to the
262 atmosphere, albeit at different time scales, 2) the area that is deforested and put under agricultural
263 use loses soil carbon and cannot sequester carbon in response to increase $[\text{CO}_2]$ since crops are
264 frequently harvested. As a result E_L is positive.

265
266 Relative to CanESM2, the version of CTEM employed in CanESM4.2, CTEM4.2, includes
267 changes to the humification factor (χ , see equations 4 and 5) which determines what fraction of
268 the humidified litter is transferred from litter (H_D) to the soil carbon pool (H_S). The value of χ
269 employed in CTEM4.2 has been changed for crop PFTs from 0.45 to 0.10, which decreases the
270 transfer of the humidified litter to the soil carbon pool. As a result, a decrease in global soil
271 carbon over the historical period is obtained as natural vegetation is replaced by croplands as is
272 seen in empirical measurements (Wei et al., 2014). This change in humification factor was
273 required despite the higher litter decomposition rates over croplands and is discussed in more
274 detail later in the results section. In addition, in CTEM4.2 the sensitivity of photosynthesis to soil
275 moisture is reduced for coupling to CLASS 3.6, especially for the broadleaf evergreen PFT
276 (which exists mainly in the tropics) to somewhat account for deep roots, for example, in the
277 Amazonian region (e.g. see da Rocha et al., 2004).

278
279 CTEM has always included a parameterization of photosynthesis down-regulation, which
280 represents acclimatization to elevated CO_2 in the form of a decline in maximum photosynthetic
281 rate. In the absence of explicit coupling of terrestrial carbon and nitrogen cycles this

282 parameterization yields a mechanism to reduce photosynthesis rates as [CO₂] increases. The
 283 photosynthesis down-regulation parameterization is described in detail in Arora et al. (2009) and
 284 is based on earlier simpler models which expressed net or gross primary productivity (NPP or
 285 GPP) as a logarithmic function of atmospheric CO₂ concentration (e.g. Cao et al., 2001;
 286 Alexandrov and Oikawa, 2002).

$$287 \quad G(t) = G_0 \left(1 + \gamma_p \ln \left(\frac{C(t)}{C_0} \right) \right) \quad (11)$$

288 where GPP at any given time, $G(t)$, is a function of its initial value G_0 , atmospheric CO₂
 289 concentration at time t , $C(t)$, and its initial value C_0 . The rate of increase of GPP is determined by
 290 the parameter γ_p (where p indicates the “potential” rate of increase of GPP with CO₂). The ratio
 291 of GPP in two different versions of a model in which GPP increases at different rates (γ_p and γ_d)
 292 is given by

$$293 \quad \xi(C) = \frac{1 + \gamma_d \ln(C/C_0)}{1 + \gamma_p \ln(C/C_0)} \quad (12)$$

294
 295 where t is omitted for clarity. When $\gamma_d < \gamma_p$, the modelled potential gross photosynthesis rate
 296 (G_p), which is not constrained by nutrient limitation, can be multiplied by the scalar $\xi(C)$
 297 (equation 12) which yields the gross primary productivity (G) used in equation (3) that now
 298 increases in response to CO₂ increases at a rate determined by the value of γ_d (the subscript d
 299 indicates down-regulation).

$$300 \quad G = \xi(C) G_p \quad (13)$$

301

302 A lower value of γ_d than γ_p yields a value of $\xi(C)$ that is less than one. As the concentration of
 303 CO_2 , expressed as C in equation (12), increases above its pre-industrial level C_0 (285 ppm), $\xi(C)$
 304 progressively decreases resulting in a gross primary productivity G , which is less than the its
 305 potential value G_p . Figure 1 shows the behaviour of $\xi(C)$ for $\gamma_p=0.95$ and three values of γ_d
 306 (0.25, 0.4 and 0.55) corresponding to three different strengths of the terrestrial CO_2 fertilization
 307 effect. A value of $\gamma_d = 0.25$ was used for CanESM2 to best simulate the globally-averaged
 308 surface CO_2 concentration and cumulative 1850-2005 atmosphere-land CO_2 flux. CanESM2,
 309 however, wasn't as rigorously evaluated as we have attempted here for CanESM4.2. Through
 310 the parameter γ_d , the physical process of down-regulation has a direct influence on the strength
 311 of the terrestrial CO_2 fertilization effect. In practice, different combinations of γ_d and γ_p are able
 312 to yield very similar values of $\xi(C)$. Arora et al. (2009) calculated the value of γ_d based on
 313 results from six studies, two of which were meta-analyses each based on 15 and 77 individual
 314 studies, that grow plants in ambient and elevated CO_2 environment. Their results are equivalent to
 315 $\gamma_d=0.46$ with a range from 0.22 to 0.63 for $\gamma_p=0.95$.

316
 317 In Figure 1, while $\xi(C)$ decreases with an increase in atmospheric CO_2 , indicating progressive
 318 decline in photosynthesis due to nutrient limitation, the slope $\frac{d\xi}{dC}$ also decreases. Although a
 319 second-order effect, this is a limitation of the current formulation of $\xi(C)$. A decreasing $\xi(C)$ as
 320 CO_2 increases can eventually also lead to decrease in GPP although we have not seen this
 321 behaviour up to CO_2 concentration of around 1000 ppm in simulations performed with CanESM2
 322 (see Arora and Boer, 2014). While γ_d is used to model down-regulation of photosynthesis it may

323 also be used as a measure of the strength of the CO₂ fertilization effect. Lower values of γ_d
324 indicate higher down-regulation (see Figure 1) so higher values of γ_d imply higher strength of the
325 CO₂ fertilization effect. Finally, γ_d is specific to CTEM and as such the value of this parameter is
326 irrelevant to other models. More relevant for comparison with other models is the simulated rate
327 of increase of NPP over the historical period that a given value of γ_d yields.

328

329 **2.2.3 Treatment of CO₂ in the atmosphere**

330

331 The land and ocean components of the carbon cycle in CanESM4.2 are operable for two
332 experimental designs – 1) an emissions-driven mode, where the atmospheric CO₂ concentration is
333 a freely evolving 3D tracer in the model and 2) a concentrations-driven mode, where the
334 atmospheric CO₂ concentration is prescribed externally.

335

336 In the emissions-driven mode the anthropogenic CO₂ emissions (E_F) are specified and since the
337 interactive land and ocean carbon cycle components simulate the F_L and F_O terms, respectively,
338 the model is able to simulate the evolution of [CO₂] through the H_A term, which represents the
339 atmospheric carbon burden, in equation (2). This is referred to as the interactively simulated
340 [CO₂], or “free-CO₂” configuration. In this case, the model simulates the transport of CO₂ in the
341 atmosphere producing 3D structure, an annual cycle, and inter-annual variability.

342

343 In the concentrations-driven mode, the land and ocean CO₂ fluxes, F_L and F_O , remain
344 interactively determined so model results can be used to diagnose the E_F term (based on equation
345 2) that is compatible with a given [CO₂] pathway at the global scale. The concentrations-driven

346 mode can be executed in two CanESM4.2 configurations. In the first configuration, a single scalar
347 value of $[\text{CO}_2]$, which may be time evolving, is imposed at all geographical and vertical locations
348 in the model. This follows the CMIP5 prescription for concentrations-driven simulations and we
349 refer to it here as, “specified-CO2” concentrations-driven mode. In the second configuration, a
350 new approach for specifying CO_2 concentration has been implemented in CanESM4.2. In this
351 new approach, only the globally averaged concentration of CO_2 in the lowest model level is
352 constrained by the prescribed value. The geographical and vertical distribution of CO_2 in the
353 atmosphere and its annual cycle in this second configuration is otherwise free to evolve in the
354 same manner as in the emissions-driven, free-CO2, configuration. A relaxation timescale of one
355 day is employed in this new configuration and a fixed annual cycle, derived from the free-CO2
356 preindustrial control simulation, is imposed on the reference value of $[\text{CO}_2]$. The reference value
357 of $[\text{CO}_2]$ may additionally be specified as time evolving. We refer to this configuration as the
358 “relaxed-CO2” concentrations-driven mode. Aside from the relaxational constraint on the global-
359 mean surface value of $[\text{CO}_2]$, the atmospheric configuration for relaxed-CO2 is identical to that
360 for free-CO2 with zero emissions. As a consequence, the relaxed CO2 configuration allows the
361 same nonlinearity in the atmosphere-surface exchange of CO_2 as the free CO2 configuration
362 leading to nearly identical spatial distribution and seasonal cycle of atmosphere CO_2
363 concentrations. In this regard, the relaxed-CO2 configuration is physically more realistic than the
364 specified-CO2 configuration.

365
366 There are practical advantages to using the relaxed-CO2 configuration over the specified-CO2
367 configuration for concentrations-driven simulations. When spinning up land and ocean carbon
368 pools in a preindustrial control simulation, the model is executed in concentrations driven mode

369 to bring these pools into equilibrium with a prescribed CO₂ concentration. In earlier versions of
370 the CanESM, a specified-CO₂ configuration was used for this purpose. Beginning with version
371 4.1, the relaxed-CO₂ configuration is used for this purpose because it produces little or no drift
372 when used to initialize the free-CO₂ preindustrial control simulations. In fact, a relaxed-CO₂
373 preindustrial control simulation may be used as the control simulation for both emissions-driven
374 and (relaxed-CO₂) concentrations-driven experiments. This is not the case when the specified-
375 CO₂ is used as the configuration for concentration driven experiments.

376

377 **3. Experimental set up**

378

379 Three different kinds of experiments are performed for this study. The first is the standard 1% per
380 year increasing CO₂ experiment (1pctCO₂) performed for three different strengths of the
381 terrestrial CO₂ fertilization effect. The 1pctCO₂ is a concentration-driven experiment and we use
382 the “relaxed-CO₂” configuration to specify CO₂ in the atmosphere. The second experiment is the
383 CMIP5 1850-2005 historical experiment, referred to as esmhistorical following CMIP5
384 terminology, which is performed with specified anthropogenic CO₂ emissions (i.e. in emissions-
385 driven, or “free-CO₂”, mode), where [CO₂] is simulated interactively. Concentrations of non-CO₂
386 greenhouse gases and emissions of aerosols and their precursors are specified in the esmhistorical
387 experiment following the CMIP5 protocol. The third experiment is same as the esmhistorical
388 experiment but LUC is not permitted and the land cover remains at its 1850 value; referred to as
389 the esmhistorical_noluc experiment. Two ensemble members are performed for each of the three
390 versions of the esmhistorical and esmhistorical_noluc experiments corresponding to three
391 different strengths of the terrestrial CO₂ fertilization effect. The rationale for performing historical

392 simulations without LUC is to be able to quantify LUC emissions E_L using equation (10). Table
393 1 summarizes all the simulations performed.

394
395 The 1pctCO2 simulations with “relaxed” CO₂ for three different strengths of the terrestrial CO₂
396 fertilization effect are initialized from a corresponding pre-industrial control simulation with CO₂
397 specified at ~285 ppm and all other forcings at their 1850 values. The esmhistorical and
398 esmhistorical_noluc simulations are initialized from a pre-industrial control simulation with
399 “free” CO₂ and zero anthropogenic CO₂ emissions.

400

401 **4. Results**

402

403 **4.1. 1% per year increasing CO₂ experiments**

404

405 Figure 2 shows the carbon budget components of equation (8); ΔH_A , ΔH_O and ΔH_L i.e. the
406 change in atmospheric carbon burden and cumulative atmosphere-ocean and atmosphere-land
407 CO₂ flux which together make up the cumulative diagnosed emissions (\tilde{E}) based on results from
408 the fully-coupled 1pctCO2 experiment. Results are shown from eight CMIP5 models that
409 participated in the Arora et al. (2013) study, including CanESM2 which used $\gamma_d=0.25$, together
410 with those from CanESM4.2 for three different strengths of the terrestrial CO₂ fertilization effect.

411 The cumulative atmosphere-land CO₂ flux across models varies much more than the cumulative
412 atmosphere-ocean CO₂ flux across the CMIP5 models as already noted in Arora et al. (2013). The
413 results for CanESM4.2 indicate that the influence of γ_d (equation 12) on the strength of the
414 model’s terrestrial CO₂ fertilization effect allows CanESM4.2’s cumulative diagnosed emissions
415 to essentially span the range of the other CMIP5 models. For the three different strengths of the

416 terrestrial CO₂ fertilization effect, $\gamma_d = 0.25, 0.4$ and 0.55 , the γ_d values of 0.4 and 0.55 yield
417 cumulative atmosphere-land CO₂ flux that is higher than all the CMIP5 models. The basis for
418 choosing these values of γ_d within the range 0.4 ± 0.15 is that they span the observation-based
419 estimates of various quantities reasonably well as shown later.

420

421 The cumulative atmosphere-land CO₂ flux ΔH_L for CanESM4.2 for the simulation with $\gamma_d=0.25$
422 is higher than that for CanESM2 which also uses $\gamma_d=0.25$, because of the changes made to soil
423 moisture sensitivity of photosynthesis and because ΔH_L also depends on the model climate. In
424 particular, the CanESM2 bias of low precipitation over the Amazonian region has been reduced
425 in CanESM4.2, as shown in Figure 3. The increased precipitation over the Amazonian region
426 causes increased carbon uptake with increasing [CO₂]. The improved precipitation bias of
427 CanESM4.2 in this region is in part caused by the decreased sensitivity of photosynthesis to soil
428 moisture in CTEM4.2, especially for broadleaf evergreen PFT, which helps to increase
429 evapotranspiration and in turn increase precipitation over the region.

430

431 **4.2. Historical simulations with LUC**

432

433 The results presented in this section evaluate the model against four observation-based
434 determinants of the global carbon cycle and the historical global carbon budget over the 1850-
435 2005 period mentioned earlier. Simulated atmosphere-ocean CO₂ fluxes are also compared with
436 observation-based estimates although, of course, they are not directly affected by the strength of
437 the terrestrial CO₂ fertilization effect.

438

439 **4.2.1. Components of land carbon budget**

440

441 In Figure 4, time series of instantaneous (F_L panel a) and cumulative (\tilde{F}_L panel b) atmosphere-
442 land CO₂ flux over the period 1850-2005 are displayed for CanESM2 (which contributed results
443 to CMIP5) and CanESM4.2 for the three different strengths of the terrestrial CO₂ fertilization
444 effect. The observation-based estimates of $F_L = (F_l - E_L)$ in Figure 4a for the decades of 1960,
445 1970, 1980, 1990 and 2000 are reproduced from Le Quéré et al. (2015) who derive the
446 $F_L = (F_l - E_L)$ term as residual of the carbon budget equation $dH_A/dt = -(F_l - E_L) - F_O + E_F$
447 using observation-based estimates of change in atmospheric carbon budget (dH_A/dt),
448 atmosphere-ocean CO₂ flux (F_O) and fossil fuel emissions (E_F). The observation-based estimate
449 of -11 ± 47 Pg C in Figure 4b for \tilde{F}_L over the period 1850-2005 is from Arora et al. (2011) (their
450 Table 1).

451

452 The primary difference between CanESM2 and CanESM4.2 simulations in Figure 4 is that \tilde{F}_L for
453 CanESM2 generally stays positive throughout the historical period, whereas for CanESM4.2 it
454 first becomes negative (indicating that land is losing carbon) and then becomes positive
455 (indicating that land is gaining carbon) towards the end of the 20th century, depending on the
456 strength of the CO₂ fertilization effect. The behaviour of \tilde{F}_L for CanESM4.2 is considered to be
457 more realistic. As the land responds to anthropogenic land use change, associated with an increase
458 in crop area early in the historical period, it causes a decrease in vegetation and soil carbon (see
459 Figure 5). Later in the 20th Century, the CO₂ fertilization effect causes the land to become a sink
460 for carbon resulting in both vegetation and soil carbon increases. This behavior is consistent with
461 the mean model response of the 15 CMIP5 models analyzed by Hoffman et al. (2013) (their

462 Figure 2b). In contrast, CanESM2 shows a gradual increase in the global soil carbon amount
463 (Figure 5a) over the historical period. In Figure 5, it can be seen that the effect of CO₂ fertilization
464 in the second half of the 20th century is delayed for soil carbon compared to that for vegetation.
465 This is primarily because of the lag introduced by the turnover time of vegetation (i.e., increased
466 NPP inputs have to go through vegetation pool first) and the longer turnover time scale of the soil
467 carbon pool. The more reasonable response of soil carbon to anthropogenic land use change, in
468 Figure 5a for CanESM4.2, is achieved by changing the humification factor from 0.45 (in
469 CanESM2) to 0.10 (in CanESM4.2) in equation (5) which yields a reduction in global soil carbon
470 amount in response to land use change up until the time that the effect of CO₂ fertilization starts
471 to take effect. In Figure 4a, CanESM4.2 is also able to simulate continuously increasing F_L during
472 the period 1960 to 2005, depending on the strength of the CO₂ fertilization effect, while
473 CanESM2 simulates near constant or decreasing F_L from about 1990 onwards, as is also seen in
474 Figure 4b for \tilde{F}_L . This behaviour of F_L is not consistent with observation-based estimates from
475 Le Quéré et al. (2015) which show continued strengthening of the land carbon sink since 1960s.
476
477 In Figure 4a, amongst the three versions of the CanESM4.2, the simulation with $\gamma_d = 0.4$ (blue
478 line) yields the best comparison with observation-based estimates of F_L from Le Quéré et al.
479 (2015), while the simulations with $\gamma_d = 0.25$ (green line) and $\gamma_d = 0.55$ (red line) yield F_L values
480 that are lower and higher, respectively, than observation-based estimates. In Figure 4b, the
481 cumulative atmosphere-land CO₂ flux \tilde{F}_L over the 1850-2005 period from the simulations with
482 $\gamma_d = 0.25$ and 0.4 (green and blue lines, respectively) lies within the uncertainty of observation-

483 based estimates, while the simulation with $\gamma_d = 0.55$ (red line) yields \tilde{F}_L value that is high
484 relative to observation-based estimate.

485
486 Figure 6 shows the change in and absolute values of NPP from CanESM2 and the simulations
487 made with CanESM4.2 for three different strengths of the CO₂ fertilization effect. Consistent with
488 1pctCO2 simulations, the rate of increase of NPP in CanESM4.2 with $\gamma_d = 0.25$ is higher than
489 that in CanESM2 which also uses $\gamma_d = 0.25$. This is because the underlying model climate is
490 different in CanESM2 and CanESM4.2, as mentioned earlier, and the fact that photosynthesis
491 sensitivity to soil moisture has also been reduced. The rates of increase of NPP for $\gamma_d = 0.40$ and
492 0.50 are, of course, even higher. The CanESM4.2 simulation with $\gamma_d = 0.40$, which yields the
493 best comparison with observation-based estimates of F_L for the decade of 1960 through 2000
494 (Figure 4a) as well as \tilde{F}_L for the period 1850-2005 (Figure 4b), yields an increase in NPP of ~16
495 Pg C/yr over the 1850-2005 period. A caveat here is that part of this increase is also caused by
496 increase in the crop area over the historical period that is realized in the model regardless of the
497 strength of the CO₂ fertilization effect. In CTEM, the maximum photosynthetic capacity of crops
498 is higher than for other PFTs to account for the fact that agricultural areas are generally fertilized.
499 As a result, increase in crop area also increases global NPP. The increasing crop productivity has
500 been suggested to contribute to the increase in amplitude of the annual [CO₂] cycle since 1960s
501 (Zeng et al., 2014). However, in the absence of an explicit representation of terrestrial N cycle
502 (and thus fertilization of cropped areas) or a representation of increase in crop yield per unit area
503 due to genetic modifications, the only processes in CTEM that contribute to changes in crop yield
504 are the change in crop area itself and the increase in crop NPP due to the CO₂ fertilization effect.

505

506 **4.2.2. Globally-averaged [CO₂]**

507

508 Figure 7 shows the simulated globally-averaged surface [CO₂] from the emissions-driven
509 esmhistorical simulation of CanESM2 and that of CanESM4.2 for three different strengths of the
510 CO₂ fertilization effect. The observation-based time series of [CO₂] is illustrated by the heavy
511 black line. The CanESM2 ($\gamma_d=0.25$) simulation yields a reasonable comparison with observation-
512 based [CO₂]. Amongst the versions of CanESM4.2 with different strengths of the CO₂
513 fertilization effect, the version with $\gamma_d=0.40$ yield the best comparison. The CanESM4.2 version
514 with $\gamma_d=0.25$ (weaker strength of the CO₂ fertilization effect) and 0.55 (stronger CO₂ fertilization
515 effect) yield CO₂ concentrations that are respectively higher and lower than the observational
516 estimate from roughly mid-20th Century onward. The reason CanESM4.2 ($\gamma_d=0.40$) requires a
517 stronger CO₂ fertilization effect than CanESM2 ($\gamma_d=0.25$) for simulating the observation-based
518 increase in atmospheric CO₂ burden over the historical period is the enhanced impact of LUC in
519 CanESM4.2 due to its increased humification factor and the associated response of the global soil
520 carbon pool, as discussed in the previous section. The differences in simulated [CO₂] in Figure 7
521 from CanESM4.2 are due only to differences in the strength of the CO₂ fertilization effect.
522 Although, of course, since in these simulations [CO₂] is simulated interactively, the simulated
523 atmosphere-land flux F_L and [CO₂] both respond to and affect each other.

524

525 Both CanESM2 and CanESM4.2 underpredict [CO₂] relative to observational estimates over the
526 period 1850-1930, and are also unable to reproduce the near zero rate of increase of [CO₂] around
527 1940. Possible reasons for these discrepancies include 1) the possibility that carbon cycle before

528 1850 was not in true equilibrium and this aspect cannot be captured since the model is spun up to
529 equilibrium for 1850 conditions, 2) the uncertainties associated with anthropogenic emissions for
530 the late 19th and early 20th century that are used to drive the model, and 3) the uncertainties
531 associated with pre Mauna-Loa [CO₂] observations.

532

533 **4.2.3. Atmosphere-ocean CO₂ flux**

534

535 Figures 8a and b, respectively, show time series of instantaneous (F_o) and cumulative (\tilde{F}_o)
536 atmosphere-ocean CO₂ fluxes over the period 1850-2005 for the set of emissions-driven
537 simulations presented in Fig. 7. The strength of the terrestrial CO₂ fertilization effect has little or
538 no impact on the ocean biogeochemical processes. The differences in values of F_o and \tilde{F}_o for
539 the three versions CanESM4.2 are, therefore, primarily due to the differences in [CO₂]. The
540 observation-based estimates of F_o in Figure 8a for the decades of 1960, 1970, 1980, 1990 and
541 2000 are from Le Quéré et al. (2015). The observation-based estimate of \tilde{F}_o of 141±27 Pg C in
542 Figure 8b for the period 1850-2005 is from Arora et al. (2011) (their Table 1).

543

544 Both CanESM2 and the CanESM4.2 simulation for $\gamma_d=0.40$ (which provides the best comparison
545 with observation-based estimate for [CO₂]; blue line in Figure 7) yield lower \tilde{F}_o compared to
546 observation-based values. The F_o value from CanESM2 and the CanESM4.2 simulation for
547 $\gamma_d=0.40$ are lower than the mean estimates from Le Quéré et al. (2015) for the decades of 1960s
548 through 2000s, although still within their uncertainty range. The family of ESMs from CCCma,
549 all of which have the same physical ocean model, including CanESM1 (Arora et al., 2009),

550 CanESM2 (Arora et al., 2011) and now CanESM4.2, yield lower than observed ocean carbon
551 uptake over the historical period. Recent analyses of these model versions suggest that the
552 primary reason for their low carbon uptake is a negative bias in near surface wind speeds over the
553 Southern Ocean and an iron limitation in the same region which is too strong (personal
554 communication, Dr. Neil Swart, Canadian Centre for Climate Modelling and Analysis). The
555 CanESM4.2 simulation with $\gamma_d=0.25$ (green line in Figure 8) yields a better comparison with
556 observation-based estimates of F_o and \tilde{F}_o but that is because of the higher simulated $[\text{CO}_2]$ in
557 that simulation associated with lower carbon uptake by land.

558

559 **4.2.4. Amplitude of the annual CO₂ cycle**

560

561 The annual CO₂ cycle is influenced strongly by the terrestrial biospheric activity of the northern
562 hemisphere (Keeling et al., 1996; Randerson et al., 1997). Higher than normal biospheric uptake
563 of carbon during a northern hemisphere's growing season, for example, will yield lower than
564 normal $[\text{CO}_2]$ by the end of the growing season, around September when $[\text{CO}_2]$ is at its lowest
565 level (see Figure 9a). Similarly, during the northern hemisphere's dormant season, increased
566 respiration from live vegetation and decomposition of dead carbon, including leaf litter, that may
567 be associated with increased carbon uptake during the last growing season, will yield higher than
568 normal $[\text{CO}_2]$ during April when $[\text{CO}_2]$ is at its highest level. Both processes increase the
569 amplitude of the annual $[\text{CO}_2]$ cycle. Given this strong control, the rate of change of the
570 amplitude of the annual $[\text{CO}_2]$ cycle can potentially help to constrain the strength of the terrestrial
571 CO₂ fertilization effect.

572

573 Figure 9a compares the annual cycle of the trend-adjusted globally-averaged near-surface
574 monthly [CO₂] anomalies from CanESM2 and the versions of CanESM4.2 for three different
575 strengths of the CO₂ fertilization effect with observation-based estimates for the 1991-2000
576 period. Figure 9b shows the time series of the amplitude of the annual cycle of the trend adjusted
577 globally-averaged near-surface monthly [CO₂] anomalies (referred to as Φ_{CO_2}) from CanESM2
578 and CanEM4.2, as well as observation-based estimates going back to 1980s. While CO₂
579 measurements at Mauna Loa started in 1959, observation-based globally-averaged near-surface
580 [CO₂] values are only available since 1980s
581 (ftp://afftp.cmdl.noaa.gov/products/trends/co2/co2_mm_gl.txt). In Figure 9b, consistent with the
582 strengthening of the CO₂ fertilization effect, associated with the increase in [CO₂], the
583 observation-based estimate of Φ_{CO_2} shows an increase from 1980s to the present. Both CanESM2
584 and versions of CanESM4.2 also show an increase in the amplitude of Φ_{CO_2} over the period
585 1850-2005. However, the absolute values of Φ_{CO_2} are lower in CanESM2 than in CanESM4.2
586 (Figure 9b). Of course, in the absence of an observation-based estimate of pre-industrial value of
587 Φ_{CO_2} it is difficult to say which value is more correct. However, when considering the present
588 day values of Φ_{CO_2} the three versions of CanESM4.2 yield better comparison with observation-
589 based estimate as also shown in Figure 9a. The increase in the value of Φ_{CO_2} from CanESM2 to
590 CanESM4.2, which now yields better comparison with observation-based value of Φ_{CO_2} , is most
591 likely caused by the change in the land surface scheme from CLASS 2.7 (that is implemented in
592 CanESM2) to CLASS 3.6 (implemented in CanESM4.2), since the atmospheric component of the
593 model hasn't changed substantially. It is, however, difficult to attribute the cause of this
594 improvement in the present day value of Φ_{CO_2} in CanESM4.2 to a particular aspect of the new

595 version of the land surface scheme. The annual [CO₂] cycle is driven primarily by the response of
596 the terrestrial biosphere to the annual cycle of temperature and the associated greening of the
597 biosphere every summer in the northern hemisphere. However, the simulated amplitude of the
598 annual cycle of near-surface temperature hasn't changed substantially from CanESM2 to
599 CanESM4.2 (not shown).

600
601 In Figure 9b, the simulated values of Φ_{CO_2} for the CanESM4.2 simulations with $\gamma_d=0.25, 0.40$
602 and 0.55 are $4.41, 4.69$ and 4.85 ppm, respectively, averaged over the period 1991-2000,
603 compared to observation-based value of Φ_{CO_2} of 4.36 ppm. Here, CanESM4.2 simulation with
604 $\gamma_d=0.25$ yields the best comparison with observation-based value of Φ_{CO_2} . An increase in the
605 strength of the CO₂ fertilization effect increases the amplitude of the annual [CO₂] cycle so a
606 larger value of γ_d yields a larger value of Φ_{CO_2} . The increase in the amplitude of the annual
607 [CO₂] cycle comes both from lower [CO₂] at the end of the growing season in September as well
608 as higher [CO₂] at the start of the northern hemisphere's growing season in April (see Figure 9a),
609 as mentioned earlier in this section.

610
611 More important than the absolute value of Φ_{CO_2} is its rate of increase over time which is a
612 measure of the strength of the terrestrial CO₂ fertilization effect. Figure 9b also shows the trend in
613 Φ_{CO_2} over the 1980-2005 overlapping period for which for both the model and observation-based
614 estimates of Φ_{CO_2} are available. The magnitude of trend for observation-based estimate of Φ_{CO_2}
615 is 0.142 ± 0.08 ppm/10-years (mean \pm standard deviation, $\bar{x} \pm \sigma_x$), implying that over the 26 year
616 1980-2005 period the amplitude of annual [CO₂] cycle has increased by 0.37 ± 0.21 ppm. The

617 calculated mean and standard deviation of the observation-based trend, however, does not take
618 into account the uncertainty associated with the observation-based estimates of $[\text{CO}_2]$,
619 consideration of which will increase the calculated standard deviation even more. The magnitudes
620 of trend in Φ_{CO_2} simulated by CanESM2 ($\gamma_d=0.25$) and CanESM4.2 (for $\gamma_d=0.25$) are
621 0.103 ± 0.05 and 0.153 ± 0.031 , respectively, and statistically not different from the trend in the
622 observation-based value of Φ_{CO_2} implying an increase of 0.27 ± 0.13 and 0.40 ± 0.08 ppm,
623 respectively, in Φ_{CO_2} over the 1980-2005 period. The statistical difference is calculated on the
624 basis of $\bar{x} \pm 1.385 \sigma_x$ range which corresponds to 83.4% confidence intervals; the estimates from
625 two sources are statistically not different at the 95% confidence level if this range overlaps (Knol
626 et al., 2011). The magnitudes of the trend in Φ_{CO_2} over the 1980-2005 period for CanESM4.2
627 simulations with $\gamma_d = 0.4$ and 0.55 (0.328 ± 0.038 and 0.314 ± 0.034 ppm/10-years, respectively)
628 are, however, more than twice, and statistically different from the observation-based estimate
629 (0.142 ± 0.08 ppm/10-years).

630
631 Overall, the CanESM4.2 simulation with $\gamma_d=0.25$ yields the amplitude of the globally-average
632 annual CO_2 cycle and its rate of increase over the 1980-2005 period that compares best with
633 observation-based estimates.

635 **4.3. Historical simulations without LUC**

636
637 Figure 10 and 11 show results from CanESM4.2 emissions-driven simulations for three different
638 strengths of the CO_2 fertilization effect that do not implement anthropogenic LUC over the
639 historical period and compare them to their corresponding simulations with LUC.

640

641 Figure 10a compares the simulated $[\text{CO}_2]$; as expected in the absence of anthropogenic LUC the
642 simulated $[\text{CO}_2]$ is lower since LUC emissions do not contribute to increase in $[\text{CO}_2]$. The
643 difference in $[\text{CO}_2]$ at the end of the simulation, in year 2005, between simulations with and
644 without LUC is 29.0, 23.6 and 19.0 ppm for $\gamma_d=0.25$, 0.40 and 0.55. The simulations with the
645 lowest strength of the CO_2 fertilization effect ($\gamma_d=0.25$) yield the largest difference because these
646 simulations also have the largest $[\text{CO}_2]$ amongst their set of simulations with and without LUC.
647 The CO_2 fertilization of the terrestrial biosphere implies that the effect of deforestation will be
648 higher, because of reduced carbon uptake by deforested vegetation, if background $[\text{CO}_2]$ is
649 higher.

650

651 Figure 10b compares the simulated NPP from CanESM4.2 simulations with and without LUC.
652 The increase in simulated NPP, regardless of the strength of the CO_2 fertilization effect, is lower
653 over the historical period in simulations without LUC for two apparent reasons. First, the rate of
654 increase of $[\text{CO}_2]$ is itself lower and second, in the absence of LUC, there is no contribution from
655 increasing crop area to NPP. Overall, the increase in NPP over the 1850-2005 period in
656 simulations with LUC is a little more than twice that in simulations without LUC. Figure 10c and
657 10d compare the changes in global vegetation biomass and soil carbon mass, over the historical
658 period, from simulations with and without LUC. As expected, in the absence of LUC, global
659 vegetation biomass and soil carbon mass more or less show a continuous increase, associated with
660 the increase in NPP which itself is due to the increase in $[\text{CO}_2]$. Consequently, in Figure 11a, the
661 cumulative atmosphere-land CO_2 flux \tilde{F}_L in simulations without LUC also shows a more or less
662 continuous increase over the historical period.

663

664 Finally, Figure 11b shows the diagnosed cumulative LUC emissions \tilde{E}_L calculated as the
665 difference between cumulative \tilde{F}_L , following equation 10, from simulations with and without
666 LUC. The diagnosed \tilde{E}_L in this manner are equal to 95, 81 and 67 Pg C, over the 1850-2005
667 period, for $\gamma_d=0.25$, 0.40 and 0.55. The calculated diagnosed \tilde{E}_L are highest for $\gamma_d=0.25$
668 associated with the highest background simulated $[\text{CO}_2]$ in these simulations, as mentioned
669 earlier. For comparison, LUC emissions estimated by Houghton (2008) for the period 1850-2005,
670 based on a book-keeping approach, are 156 Pg C but these estimates are generally believed to be
671 $\pm 50\%$ uncertain (see Figure 1 of Ramankutty et al. (2007)). LUC emissions, when calculated by
672 differencing F_L from simulations with and without LUC, also depend on the type of simulations
673 performed - in particular, if simulations are driven with specified CO_2 concentrations or specified
674 CO_2 emissions. Had our simulations been concentration-driven, in contrast to being emissions
675 driven, then both with and without LUC simulations would have experienced the same specified
676 observed CO_2 concentration over the historical period and the simulated LUC emissions would
677 have been higher. Arora and Boer (2010) found that diagnosed LUC emissions in the first version
678 of the Canadian Earth System Model (CanESM1) increased from 71 Pg C (for emissions-driven
679 simulations) to 124 Pg C (for concentration-driven simulations). Concentration-driven
680 simulations, however, cannot be evaluated against observation-based amplitude of the annual CO_2
681 cycle and its increase over the historical period. These simulations either ignore the annual cycle
682 of CO_2 (our specified- CO_2 case) or use a specified amplitude of the CO_2 annual cycle (our
683 relaxed- CO_2 case).

684

685 **5.0. Discussion and conclusions**

686

687 This study evaluates the ability of four observation-based determinants of the global carbon cycle
688 and the historical carbon budget to constrain the parameterization of photosynthesis down-
689 regulation, which directly determines the strength of the CO₂ fertilization effect, over the
690 historical period 1850-2005. The key parameter that controls the strength of the CO₂ fertilization
691 effect in CTEM, γ_d , was varied in the latest version of CCCma's earth system model CanESM4.2.
692 Comparing simulated and observation-based estimates of 1) globally-averaged atmospheric CO₂
693 concentration, 2) cumulative atmosphere-land CO₂ flux, and 3) atmosphere-land CO₂ flux for the
694 decades of 1960s, 1970s, 1980s, 1990s and 2000s, it is found that the CanESM4.2 version with
695 $\gamma_d=0.40$ yields the best comparison.

696

697 The evaluation of CTEM within the framework of CanESM4.2 presented here is based on an
698 emergent model property at the global scale and may be considered as a top-down approach of
699 model evaluation. In contrast, the bottom-up approaches of model evaluation typically evaluate
700 model results and processes against observations of primary atmosphere-land carbon and/or
701 nitrogen fluxes and sizes of the vegetation, litter and soil carbon/nitrogen pools (e.g. Zaehle et
702 al., 2014). Indeed, CTEM has been evaluated at point (e.g. Arora and Boer, 2005; Melton et al.,
703 2015), regional (e.g. Peng et al., 2014; Garnaud et al., 2014) and global (e.g. Arora and Boer,
704 2010; Melton and Arora, 2014) scales in a number of studies when driven with observation-based
705 reanalysis data. Both top-down and bottom-up approaches of model evaluation are complimentary
706 to each other and allow to evaluate different aspects of the model at different spatial and temporal
707 scales.

708

709 For the top-down approach used here, CanESM4.2 simulates globally-averaged near-surface
710 [CO₂] of 400, **381** and 368 ppm for $\gamma_d=0.25$, **0.40** and 0.55, respectively, compared to the
711 observation-based estimate of **379** ppm for year 2005. The cumulative atmosphere-land CO₂ flux
712 of 18 Pg C for the period 1850-2005 for $\gamma_d=0.40$ lies within the range of the observation-based
713 estimate of -11 ± 47 Pg C in Figure 4b, and so do the average atmosphere-land CO₂ flux for the
714 decades of 1960s through to 2000s in Figure 4a when compared to observation-based estimates
715 from Le Quéré et al. (2015). $\gamma_d=0.25$ and 0.55 yield average atmosphere-land CO₂ flux for the
716 decades of 1960s through to 2000s that are lower and higher, respectively, than the observation-
717 based estimates from Le Quéré et al. (2015). The only determinant against which $\gamma_d=0.40$ does
718 not yield the best comparison with observation-based estimates is the amplitude of the globally-
719 averaged annual CO₂ cycle and its increase over the 1980 to 2005 period. For this determinant,
720 $\gamma_d=0.25$ seems to yield the best comparison (Figure 9). The value of $\gamma_d=0.40$ that yields best
721 overall comparison with observation-based determinants of the global carbon cycle and the
722 historical carbon budget is also broadly consistent with Arora et al. (2009) who derived a value of
723 $\gamma_d=0.46$ based on results from FACE studies (as mentioned in Section 2.2.2).

724

725 The caveat with the analyses presented here, or for any model for that matter, is that the strength
726 of the terrestrial CO₂ fertilization effect is dependent on the processes included in the model and
727 the parameter values associated with them. The primary example of this is the adjustment to the
728 humification factor in CTEM4.2, which leads to reduction in the global soil carbon amount as
729 anthropogenic LUC becomes significant towards the mid-20th Century. This response of soil
730 carbon was not present in the model's configuration of CTEM and historical simulations made
731 with CanESM2. The representation of soil carbon loss, in response to anthropogenic LUC in

732 CanESM4.2, implies that a stronger CO₂ fertilization effect (or weaker photosynthesis down-
733 regulation) should be required to reproduce realistic atmosphere-land CO₂ flux over the historical
734 period and this was found to be the case in Figure 4a. Despite this dependence on processes
735 included in the model, the response of the land carbon cycle, over the historical period, to the two
736 primary forcings of increased [CO₂] and anthropogenic land use change must be sufficiently
737 realistic in the model to satisfy all the four determinants of the global carbon cycle and the
738 historical global carbon budget.

739
740 The simulated loss in soil carbon in response to anthropogenic LUC over the historical period
741 may also be assessed against observation-based estimates from Wei et al. (2014). Using data from
742 453 sites that were converted from forest to agricultural land, Wei et al. (2014) find that the soil
743 organic carbon stocks decreased by an average of $43.1 \pm 1.1\%$ for all sites. Based on the HYDE
744 v3.1 data set from which the changes in crop area are derived (Hurtt et al., 2011), LUC as
745 implemented in CanESM4.2 yields an increase in crop area from about 5 million km² in 1850 to
746 about 15 million km² in 2005. Assuming an initial soil carbon amount of 10 Kg C/m² (see Figure
747 2c of Melton and Arora (2014)) and an average 40% decrease in soil carbon amount, based on
748 Wei et al. (2014), implies that the increase in crop area of about 10 million km² over the historical
749 period has likely yielded a global soil organic carbon loss of 40 Pg C. The loss in soil carbon in
750 Figure 5a is simulated to 18 Pg C for CanESM4.2 simulation with $\gamma_d = 0.40$, the simulation that
751 yield best comparison with observation-based determinants of the global carbon cycle and the
752 historical carbon budget. This loss of 18 Pg C is expected to be less than the 40 Pg C because the
753 model estimates also include an increase associated with the increase in NPP due to the CO₂
754 fertilization effect from non-crop areas. The effect of LUC on global soil carbon loss may also by

755 estimated by differencing global soil carbon amounts from simulations with and without LUC
756 from Figure 10d at the end of the simulation in year 2005. For CanESM4.2 simulation with $\gamma_d =$
757 0.40, this amounts to around 50 Pg C. Both these estimates of soil carbon loss are broadly
758 consistent with the back-of-the-envelope calculation of 40 Pg C soil carbon loss, based on Wei et
759 al. (2014) estimates, indicating that the soil carbon loss simulated in response to anthropogenic
760 LUC over the historical period is not grossly over or underestimated.

761
762 The CanESM4.2 simulation with $\gamma_d = 0.40$, however, fails to satisfy the rate of increase of the
763 amplitude of the globally-averaged annual CO₂ cycle over the 1980-2005 period implying that
764 there are still limitations in the model structure and/or parameter values. Of course, the fact that
765 the amplitude of the globally-averaged annual CO₂ cycle is also affected by the atmosphere-ocean
766 CO₂ fluxes makes it more difficult to attribute the changes in the amplitude of the globally-
767 averaged annual CO₂ cycle solely to atmosphere-land CO₂ fluxes. Additionally, the increase in
768 crop area as well as crop yield per unit area over the historical period have been suggested by
769 Zeng et al. (2014) to contribute towards the observed increase in the amplitude of annual CO₂
770 cycle. Based on their sensitivity tests, Zeng et al. (2014) attribute 45, 29 and 26 percent of the
771 observed increase in the seasonal-cycle amplitude of the CO₂ cycle to LUC, climate variability
772 and change (including factors such as the lengthening of the growing season) and increased
773 productivity due to CO₂ fertilization, respectively. Comparison of the rate of increase of NPP in
774 CanESM4.2 experiments with and without LUC (Figure 10b), as a measure of increase in the
775 strength of the CO₂ fertilization effect, suggests that the contribution of anthropogenic LUC to the
776 increase in the seasonal-cycle amplitude is 52%, which is broadly consistent with the 45% value
777 obtained by Zeng et al. (2014).

778

779 While CanESM4.2 simulation with $\gamma_d=0.40$ is able to simulate a realistic rate of increase of
780 $[\text{CO}_2]$ over the period 1960 to 2005, the modelled atmosphere-ocean CO_2 fluxes for this and the
781 CanESM2 version are lower than observational estimates of this quantity (Figure 8). This implies
782 that if the modelled atmosphere-ocean CO_2 flux were to increase and become more consistent
783 with observation-based estimates then the modelled atmosphere-land CO_2 flux must decrease to
784 still be able to yield sufficiently realistic rate of increase of $[\text{CO}_2]$. This implies that the strength
785 of the terrestrial CO_2 fertilization effect should likely be somewhat lower than what is obtained by
786 $\gamma_d=0.40$ or the simulated atmosphere-land CO_2 flux is higher because of some other reason, most
787 likely lower LUC emissions. Indeed, the required decrease in modelled atmosphere-land CO_2 flux
788 is consistent with the fact that the modelled LUC emissions for $\gamma_d=0.40$ (81 Pg C) are about half
789 the estimate from Houghton (2008) (156 Pg C) with the caveat, of course, that Houghton's
790 estimates themselves have an uncertainty of roughly $\pm 50\%$. The LUC module of CTEM currently
791 only accounts for changes in crop area and does not take into account changes associated with
792 pasture area given their ambiguous definition (pasture may or may not be grasslands). The model
793 also does not take into account wood harvesting which amongst other uses is also used as a
794 biofuel. Treatment of these additional processes will increase modelled LUC emissions.

795

796 Although the CanESM4.2 simulation with $\gamma_d=0.40$ satisfies three out of four constraints placed
797 by the chosen determinants of the global carbon cycle and the historical carbon budget, and also
798 simulates reasonable soil carbon loss in response to anthropogenic LUC, the model now yields
799 the highest land carbon uptake, in the 1pctCO2 experiment, amongst the CMIP5 models that were
800 compared by Arora et al. (2013) as seen in Figure 2. Of course, the 1pctCO2 experiment is in no

801 way indicative of models' performance over the historical period, nor is being an outlier amongst
802 CMIP5 models a conclusive evaluation of CanESM4.2's land carbon uptake. However, it remains
803 possible that the chosen determinants of the global carbon cycle and the historical carbon budget
804 are not able to constrain the model sufficiently, given the especially large uncertainty associated
805 with LUC emissions. Nevertheless, these observation-based constraints of the carbon cycle and
806 historical carbon budget are essentially the only means to evaluate carbon cycle aspects of the
807 ESMs at the global scale including the strength of the terrestrial CO₂ fertilization effect. In the
808 near future, availability of model output from the sixth phase of CMIP (CMIP6) will allow a
809 comparison of the simulated aspects of the global carbon cycle and the historical carbon budget
810 from ESMs to observations-based estimates for the 1850-2014 period. These data will allow a
811 comparison of the rate of increase of the amplitude of globally-averaged surface [CO₂] in models
812 with observation-based estimates over a longer period. This should help better constrain the
813 strength of the terrestrial CO₂ fertilization effect, as it is represented in models, in a somewhat
814 more robust manner.

815

816 **6.0 Source code and data availability**

817 Source code for the complete CanESM4.2 model is an extremely complex set of FORTRAN
818 subroutines, with C preprocessor (CPP) directives, that reside in CCCma libraries. Unix shell
819 scripts process the model code for compilation based on CPP directives and several other
820 switches (e.g. those related to free-CO₂, specified-CO₂, and relaxed-CO₂ settings). As such, it is
821 extremely difficult to make the full model code available. However, selected model subroutines
822 related to specific physical and biogeochemical processes can be made available by either author
823 (vivek.arora@canada.ca, john.scinocca@canada.ca) upon agreeing to Environment and Climate

824 Change Canada's software licensing agreement available at
825 <http://collaboration.cmc.ec.gc.ca/science/rpn.comm/license.html>. Data used to produce plots and
826 figures can be obtained from the first author (vivek.arora@canada.ca).

827

828 **Copyright statement**

829 The works published in this journal are distributed under the Creative Commons Attribution 3.0
830 License. This license does not affect this Crown copyright work, which is re-usable under the
831 Open Government License (OGL). The Creative Commons Attribution 3.0 License and the OGL
832 are interoperable and do not conflict with, reduce or limit each other. ©Crown copyright 2015.

833

834 **Acknowledgements**

835 We would like to thank Joe Melton and Neil Swart for providing comments on an earlier version
836 of this paper. We also thank the three anonymous reviewers for their constructive and helpful
837 comments.

838

839 **References**

- 840 Arora, V. K. and Boer, G. J. (2005) A parameterization of leaf phenology for the terrestrial ecosystem
841 component of climate models, *Glob. Change Biol.*, 11, 39–59, doi:10.1111/j.1365-
842 2486.2004.00890.x.
- 843 Arora, V. K. and Boer, G. J. (2014) Terrestrial ecosystems response to future changes in climate and
844 atmospheric CO₂ concentration, *Biogeosciences*, 11, 4157-4171, doi:10.5194/bg-11-
845 4157-2014 Arora, V. K. and Boer, G. J. (2014) Terrestrial ecosystems response to future
846 changes in climate and atmospheric CO₂ concentration, *Biogeosciences Discuss.*, 11,
847 3581-3614, doi:10.5194/bgd-11-3581-2014.
- 848 Arora, V. K., G. J. Boer, J. R. Christian, C. L. Curry, K. L. Denman, K. Zahariev, G. M. Flato, J. F.
849 Scinocca, W. J. Merryfield, and W. G. Lee (2009) The effect of terrestrial photosynthesis
850 down-regulation on the 20th century carbon budget simulated with the CCCma Earth
851 System Model, *J. Clim.*, 22, 6066-6088.
- 852 Arora, V. K., G. J. Boer, P. Friedlingstein, M. Eby, C. D. Jones, J. R. Christian, G. Bonan, L. Bopp,
853 V. Brovkin, P. Cadule, T. Hajima, T. Ilyina, K. Lindsay, J. F. Tjiputra, T. Wu (2013)
854 Carbon-Concentration and Carbon-Climate Feedbacks in CMIP5 Earth System Models.
855 *Journal of Climate*, Vol. 26, Iss. 15, pp. 5289-5314.
- 856 Arora, V. K., J. F. Scinocca, G. J. Boer, J. R. Christian, K. L. Denman, G. M. Flato, V. V. Kharin, W.
857 G. Lee, and W. J. Merryfield (2011) Carbon emission limits required to satisfy future
858 representative concentration pathways of greenhouse gases, *Geophys. Res. Lett.*, 38,
859 L05805, doi:10.1029/2010GL046270.
- 860 Arora, V.K. and G.J. Boer (2010) Uncertainties in the 20th century carbon budget associated with
861 land use change, *Global Change Biology*, 16(12), 3327-3348.
- 862 Bartlett, P. A., Mackay, M. D., and Verseghy, D. L. (2006) Modified snow algorithms in the Canadian
863 Land Surface Scheme: model runs and sensitivity analysis at three boreal forest stands,
864 *Atmos. Ocean*, 44, 207–222.
- 865 Bartlett, P. and Verseghy, D. (2015) Modified treatment of intercepted snow improves the
866 simulated forest albedo in the Canadian Land Surface Scheme, *Hydrol. Process.*, 29, 3208–
867 3226, doi:10.1002/hyp.10431.
- 868 Brown, R., Bartlett, P., Mackay, M., and Verseghy, D. (2006) Estimation of snow cover in CLASS for
869 SnowMIP, *Atmos. Ocean*, 44, 223–238.

870 Christian, J. R., and coauthors (2010) The global carbon cycle in the Canadian Earth system model
871 (CanESM1): Preindustrial control simulation, *J. Geophys. Res.*, 115, G03014,
872 doi:10.1029/2008JG000920.

873 Ciais, P., C. Sabine, G. Bala, L. Bopp, V. Brovkin, J. Canadell, A. Chhabra, R. DeFries, J. Galloway,
874 M. Heimann, C. Jones, C. Le Quéré, R.B. Myneni, S. Piao and P. Thornton (2013) Carbon
875 and Other Biogeochemical Cycles. In: *Climate Change 2013: The Physical Science Basis.*
876 *Contribution of Working Group I to the Fifth Assessment Report of the Intergovernmental*
877 *Panel on Climate Change* [Stocker, T.F., D. Qin, G.-K. Plattner, M. Tignor, S.K. Allen, J.
878 Boschung, A. Nauels, Y. Xia, V. Bex and P.M. Midgley (eds.)]. Cambridge University
879 Press, Cambridge, United Kingdom and New York, NY, USA.

880 da Rocha, H.R., M.L. Goulden, S.D. Miller, M.C. Menton, L.D.V.O. Pinto, H.C. De Freitas, and
881 A.M.E. Silva Figueira (2004): Seasonality of water and heat fluxes over a tropical forest
882 in eastern Amazonia, *Ecological Applications*, 14(4) Supplement, S22-S32.

883 Friedlingstein, P., P. Cox, R. Betts, L. Bopp, W. von Bloh, V. Brovkin, P. Cadule, S. Doney, M. Eby,
884 I. Fung, G. Bala, J. John, C. Jones, F. Joos, T. Kato, M. Kawamiya, W. Knorr, K. Lindsay,
885 H. D. Matthews, T. Raddatz, P. Rayner, C. Reick, E. Roeckner, K.-G. Schnitzler, R.
886 Schnur, K. Strassmann, A. J. Weaver, C. Yoshikawa, N. Zeng. 2006: Climate–carbon
887 cycle feedback analysis: Results from the C4MIP model intercomparison, *J. Clim.*, 19(14),
888 3337-3353.

889 G. C. Hurtt, L. P. Chini, S. Frohking, R. A. Betts, J. Feddema, G. Fischer, J. P. Fisk, K. Hibbard, R. A.
890 Houghton, A. Janetos, C. D. Jones, G. Kindermann, T. Kinoshita, Kees Klein Goldewijk,
891 K. Riahi, E. Shevliakova, S. Smith, E. Stehfest, A. Thomson, P. Thornton, D. P. van
892 Vuuren, Y. P. Wang (2011) Harmonization of land-use scenarios for the period 1500-
893 2100: 600 years of global gridded annual land-use transitions, wood harvest, and resulting
894 secondary lands. *Climatic Change*, 109, 117-161, doi:10.1007/s10584-011-0153-2.

895 Garnaud, C., L. Sushama, V. K. Arora (2014) The effect of driving climate data on the simulated
896 terrestrial carbon pools and fluxes over North America, *International Journal of*
897 *Climatology* 34 (4), 1098-1110.

898 Gillett, N. P., V. K. Arora, D. Matthews, M. R. Allen (2013) Constraining the Ratio of Global
899 Warming to Cumulative CO₂ Emissions Using CMIP5 Simulations. *Journal of Climate*,
900 Vol. 26, Iss. 18, pp. 6844-6858.

901 Gourджи, S. M., K. L. Mueller, V. Yadav, D. N. Huntzinger, A. E. Andrews, M. Trudeau, G. Petron, T.
902 Nehr Korn, J. Eluszkiewicz, J. Henderson, D. Wen, J. Lin, M. Fischer, C. Sweeney, and A.
903 M. Michalak (2012) North American CO₂ exchange: inter-comparison of modeled
904 estimates with results from a fine-scale atmospheric inversion, *Biogeosciences*, 9, 457–
905 475, doi:10.5194/bg-9-457-2012.

906 Hoffman, F. M., J. T. Randerson, V. K. Arora, Q. Bao, P. Cadule, D. Ji, C. D. Jones, M. Kawamiya,
907 S. Khatiwala, K. Lindsay, A. Obata, E. Shevliakova, K. D. Six, J. F. Tjiputra, E. M.
908 Volodin, and T. Wu (2014) Causes and implications of persistent atmospheric
909 carbondioxide biases in Earth System Models, *J. Geophys. Res. Biogeosci.*, 119, 141–162,
910 doi:10.1002/2013JG002381.

911 Houghton, R.A. 2008. Carbon Flux to the Atmosphere from Land-Use Changes: 1850-2005. In
912 *TRENDS: A Compendium of Data on Global Change*. Carbon Dioxide Information
913 Analysis Center, Oak Ridge National Laboratory, U.S. Department of Energy, Oak Ridge,
914 Tenn., U.S.A.

915 Jones, C., E. Robertson, V. Arora, P. Friedlingstein, E. Shevliakova, L. Bopp, V. Brovkin, T. Hajima,
916 E. Kato, M. Kawamiya, S. Liddicoat, K. Lindsay, C.H. Reick, C. Roelandt, J.
917 Segschneider, J. Tjiputra (2013) Twenty-First-Century Compatible CO₂ Emissions and
918 Airborne Fraction Simulated by CMIP5 Earth System Models under Four Representative
919 Concentration Pathways. *Journal of Climate*, Vol. 26, Iss. 13, pp. 4398-4413.

920 Keeling, C. D., Chin, J. F. S. & Whorf, T. P. (1996) Increased activity of northern vegetation inferred
921 from atmospheric CO₂ measurements. *Nature* 382, 146–149.

922 Khatiwala, S., F. Primeau, and T. Hall (2009) Reconstruction of the history of anthropogenic CO₂
923 concentrations in the ocean. *Nature*, 462, 346–349.

924 Knol, M. J., W. R. Pestman, and D. E. Grobbee (2011) The (mis)use of overlap of confidence
925 intervals to assess effect modification, *Eur. J. Epidemiol.*, 26(4), 253–254.

926 Knorr, W. (2009) Is the airborne fraction of anthropogenic CO₂ emissions increasing?, *Geophys. Res.*
927 *Lett.*, 36, L21710, doi:10.1029/2009GL040613.

928 Le Quéré, C., Moriarty, R., Andrew, R. M., Peters, G. P., Ciais, P., Friedlingstein, P., Jones, S. D.,
929 Sitch, S., Tans, P., Arneeth, A., Boden, T. A., Bopp, L., Bozec, Y., Canadell, J. G., Chini,
930 L. P., Chevallier, F., Cosca, C. E., Harris, I., Hoppema, M., Houghton, R. A., House, J. I.,
931 Jain, A. K., Johannessen, T., Kato, E., Keeling, R. F., Kitidis, V., Klein Goldewijk, K.,
932 Koven, C., Landa, C. S., Landschützer, P., Lenton, A., Lima, I. D., Marland, G., Mathis, J.

933 T., Metzl, N., Nojiri, Y., Olsen, A., Ono, T., Peng, S., Peters, W., Pfeil, B., Poulter, B.,
934 Raupach, M. R., Regnier, P., Rödenbeck, C., Saito, S., Salisbury, J. E., Schuster, U.,
935 Schwinger, J., Séférian, R., Segschneider, J., Steinhoff, T., Stocker, B. D., Sutton, A. J.,
936 Takahashi, T., Tilbrook, B., van der Werf, G. R., Viovy, N., Wang, Y.-P., Wanninkhof,
937 R., Wiltshire, A., and Zeng, N. (2015) Global carbon budget 2014, *Earth Syst. Sci. Data*,
938 7, 47-85, doi:10.5194/essd-7-47-2015.

939 Ma, X., von Salzen, K., and Li, J. (2008) Modelling sea salt aerosol and its direct and indirect effects
940 on climate, *Atmos. Chem. Phys.*, 8, 1311–1327, doi:10.5194/acp-8-1311-2008.

941 McGuire, A. D., J. M. Melilli, and L. A. Joyce (1995): The role of nitrogen in the response of forest
942 net primary productivity to elevated atmospheric carbon dioxide, *Annual Reviews of*
943 *Ecology and Systematics*, 26, 473-503.

944 Medlyn, B. E., F. -W. Badeck, D. G. G. De Pury, C. V. M. Barton, M. Broadmeadow, R. Ceulemans,
945 P. De Angelis, M. Forstreuter, M. E. Jach, S. Kellomäki, E. Laitat, M. Marek, S. Philippot,
946 A. Rey, J. Strassmeyer, K. Laitinen, R. Liozon, B. Portier, P. Roberntz, K. Wang, P. G.
947 Jstbid (1999): Effects of elevated [CO₂] on photosynthesis in European forest species: a
948 meta-analysis of model parameters, *Plant, Cell & Environment*, 22, 1475–1495.

949 Melton, J. R. and Arora, V. K. (2014) Sub-grid scale representation of vegetation in global land
950 surface schemes: implications for estimation of the terrestrial carbon sink, *Biogeosciences*,
951 11, 1021-1036, doi:10.5194/bg-11-1021-2014.

952 Melton, J. R. and Arora, V. K. (2014) Sub-grid scale representation of vegetation in global land
953 surface schemes: implications for estimation of the terrestrial carbon sink, *Biogeosciences*,
954 11, 1021-1036, doi:10.5194/bg-11-1021-2014.

955 Melton, J. R., Shrestha, R. K., and Arora, V. K. (2015) The influence of soils on heterotrophic
956 respiration exerts a strong control on net ecosystem productivity in seasonally dry
957 Amazonian forests, *Biogeosciences*, 12, 1151-1168, doi:10.5194/bg-12-1151-2015.

958 Namazi, M., von Salzen, K., and Cole, J. N. S. (2015) Simulation of black carbon in snow and its
959 climate impact in the Canadian Global Climate Model, *Atmos. Chem. Phys. Discuss.*, 15,
960 18839-18882, doi:10.5194/acpd-15-18839-2015.

961 Peng, Y., Arora, V. K., Kurz, W. A., Hember, R. A., Hawkins, B. J., Fyfe, J. C., and Werner, A. T.
962 (2014) Climate and atmospheric drivers of historical terrestrial carbon uptake in the
963 province of British Columbia, Canada, *Biogeosciences*, 11, 635-649, doi:10.5194/bg-11-
964 635-2014.

965 Peng, Y., von Salzen, K., and Li, J. (2012) Simulation of mineral dust aerosol with Piecewise Log-
966 normal Approximation (PLA) in CanAM4-PAM, *Atmos. Chem. Phys.*, 12, 6891–6914, 30
967 doi:10.5194/acp-12-6891-2012.

968 Phillips, O. L. and S. L. Lewis (2014) Evaluating the tropical forest carbon sink, *Global Change*
969 *Biology* (2014) 20, 2039–2041, doi: 10.1111/gcb.12423.

970 Pongratz, J., Reick, C. H., Houghton, R. A., and House, J. I. (2014) Terminology as a key uncertainty
971 in net land use and land cover change carbon flux estimates, *Earth Syst. Dynam.*, 5, 177-
972 195, doi:10.5194/esd-5-177-2014.

973 Ramankutty, N., H. K. Gibbs, F. Archard, R. DeFries, J. A. Foley, and R. A. Houghton (2007):
974 Challenges to estimating carbon emissions from tropical deforestation , *Global Change*
975 *Biology*, 13(1), 51-66.

976 Randerson, J. T., Thompson, M. V., Conway, T. J., Fung, I. Y. & Field, C. B. (1997) The contribution
977 of terrestrial sources and sinks to trends in the seasonal cycle of atmospheric carbon
978 dioxide. *Glob. Biogeochem. Cycles* 11, 535–560.

979 Schimel, D., Stephens, B. B., and Fisher, J. B.: Effect of increasing CO₂ on the terrestrial carbon
980 cycle (2015) *Proceedings of the National Academy of Science U.S.A.*, 112, 436–441,
981 doi:10.1073/pnas.1407302112, 2015.

982 Sturm, M., Holmgren, J., König, M., and Morris, K. (1997) The thermal conductivity of seasonal
983 snow, *J. Glaciol.*, 43, 26–41.

984 Tabler, R. D., Benson, C. S., Santana, B. W., and Ganguly, P. (1990) Estimating snow transport from
985 30 wind speed records: estimates versus measurements at Prudhoe Bay, Alaska, in: *Proc.*
986 *58th Western Snow Conf.*, Sacramento, CA, 61–78.

987 Taylor, Karl E., Ronald J. Stouffer, Gerald A. Meehl, 2012: An Overview of CMIP5 and the
988 Experiment Design. *Bull. Amer. Meteor. Soc.*, 93, 485–498.

989 Verseghy, D. L. (2012) CLASS-the Canadian land surface scheme (version 3.6)—technical
990 documentation. Internal report, Climate Research Division, Science and Technology
991 Branch, Environment Canada (Downsview, Toronto, Ontario)

992 von Salzen, K. (2006) Piecewise log-normal approximation of size distributions for aerosol
993 modelling, *Atmos. Chem. Phys.*, 6, 1351–1372, doi:10.5194/acp-6-1351-2006.

994 von Salzen, K., and Coauthors, 2013: The Canadian fourth generation atmospheric global climate
995 model (CanAM4). Part I: Representation of physical processes. *Atmos. Ocean*, 51,
996 doi:10.1080/07055900.2012.75561.

997 Wei, X., M. Shao, W. Gale and L. Li (2014) Global pattern of soil carbon losses due to the conversion
998 of forests to agricultural land, *Scientific Reports* 4, Article number: 4062 (2014)
999 doi:10.1038/srep04062.

1000 Zaehle, S., Medlyn, B. E., De Kauwe, M. G., Walker, A. P., Dietze, M. C., Hickler, T., Luo, Y.,
1001 Wang, Y.-P., El-Masri, B., Thornton, P., Jain, A., Wang, S., Warlind, D., Weng, E.,
1002 Parton, W., Iversen, C. M., Gallet-Budynek, A., McCarthy, H., Finzi, A., Hanson, P. J.,
1003 Prentice, I. C., Oren, R., and Norby, R. (2014) Evaluation of 11 terrestrial carbon–nitrogen
1004 cycle models against observations from two temperate Free-Air CO₂ Enrichment studies,
1005 *New Phytologist*, 202, 803–822, doi:10.1111/nph.12697.

1006 Zeng, N., Zhao, F., Collatz, G. J., Kalnay, E., Salawitch, R. J., West, T. O., Guanter, L. (2014) .
1007 Agricultural Green Revolution as a driver of increasing atmospheric CO₂ seasonal
1008 amplitude, *Nature*, 515(7527), 394-397.

1009 Zobler, L. 1986. A World Soil File for Global Climate Modelling. NASA Technical Memorandum
1010 87802. NASA Goddard Institute for Space Studies, New York, New York, U.S.A.
1011

1012

1013 Table 1: Summary of simulations performed for this study and the forcings used.

Simulation	1pctCO2	esmhistorical	esmhistorical_noluc
Simulation details	1% per year increasing CO ₂ simulation	1850-2005 historical simulation based on CMIP5 protocol	1850-2005 historical simulation based on CMIP5 protocol, but with no anthropogenic land use change
Purpose	To allow comparison of CanESM4.2 with CMIP5 models especially in terms of its land carbon uptake	To compare simulated aspects of the global carbon cycle and historical carbon budget with observation-based estimates	To diagnose LUC emissions by differencing atmosphere-land CO ₂ flux between historical simulations with and without LUC.
Length	140 years	156 years	
CO ₂ forcing	285 ppm at the start of the simulation and 1140 ppm after 140 years.	Historical CO ₂ forcing	
Land cover forcing	Land cover corresponds to its 1850 state	Land cover evolution is based on increase in crop area over the historical period	Land cover corresponds to its 1850 state
Non-CO ₂ greenhouse gases forcing	Concentration of non-CO ₂ GHGs is specified at their 1850 levels.	Concentration of non-CO ₂ GHGs is specified and evolves over the historical period based on the CMIP5 protocol	
Aerosols forcing	Emissions of aerosols and their precursors are specified at their 1850 levels.	Emissions of aerosols and their precursors are specified and evolve over the historical period based on the CMIP5 protocol	

1014

1015

1016

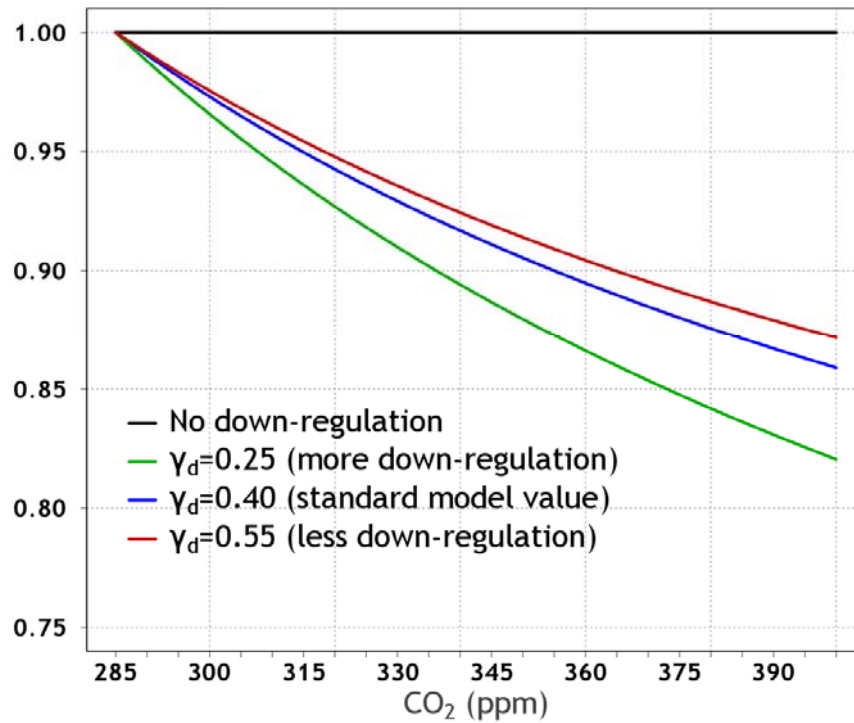
1017

1018

1019

1020

Down-regulation factor as a function of CO₂ concentration



1021

1022 Figure 1: The behaviour of terrestrial photosynthesis down-regulation scalar $\xi(C)$ (equation 12)

1023 for $\gamma_p=0.95$ and values of γ_d equal to 0.25, 0.4 and 0.55 that are used in CanESM4.2 simulations.

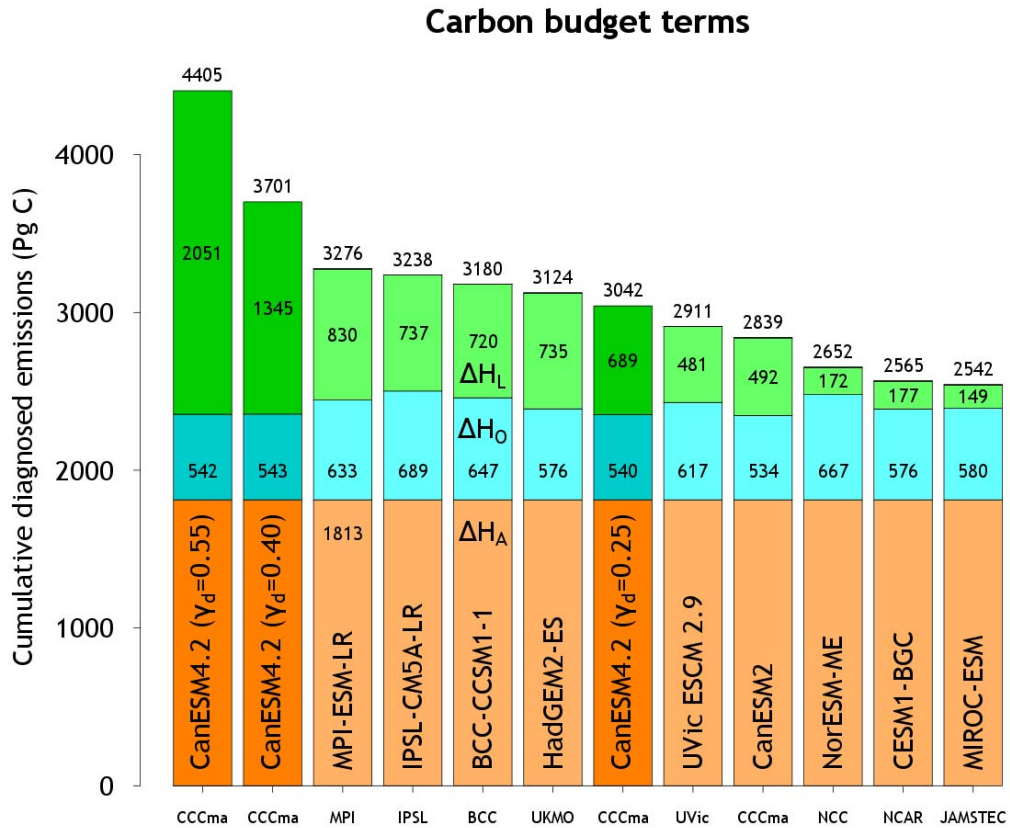
1024

1025

1026

1027

1028



1029

1030

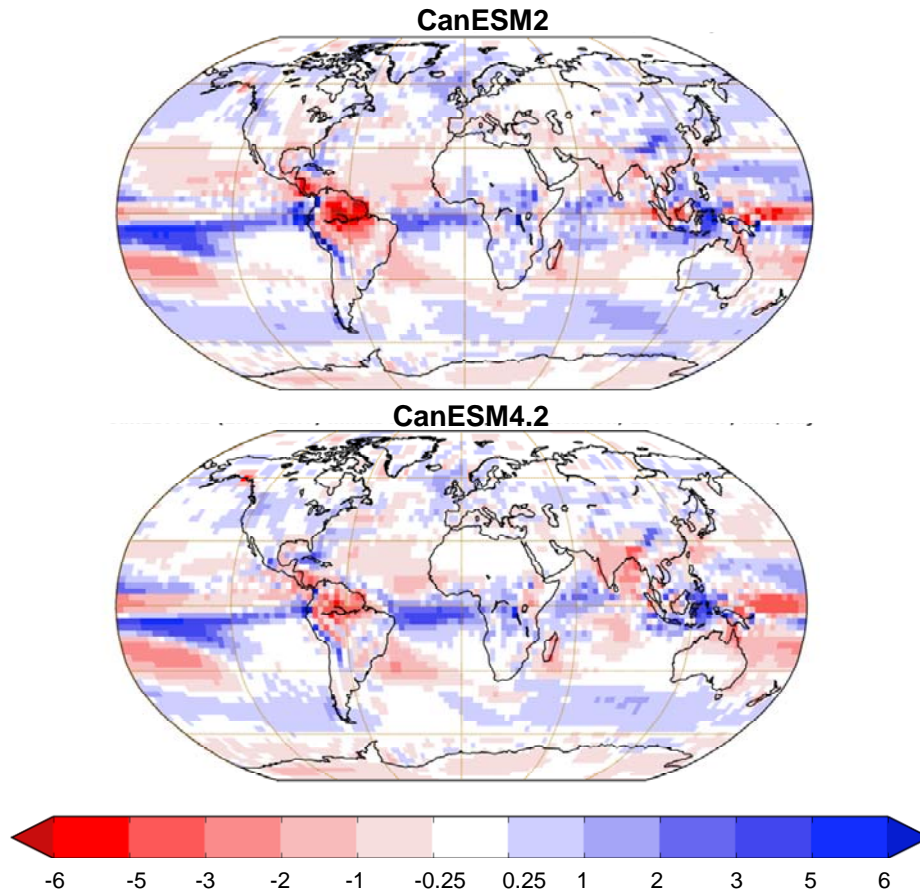
1031 Figure 2: Components of the carbon budget equation (8) that make up cumulative diagnosed
 1032 emissions based on results from the fully-coupled 1pctCO₂ experiment. Results shown are from
 1033 eight CMIP5 models that participated in the Arora et al. (2013) study and from three CanESM4.2
 1034 simulations (shown in darker colours) for three different strengths of the terrestrial CO₂
 1035 fertilization effect.

1036

1037

1038

Model minus Xie and Arkin precipitation
averaged over the 1979-1998 period (mm/day)

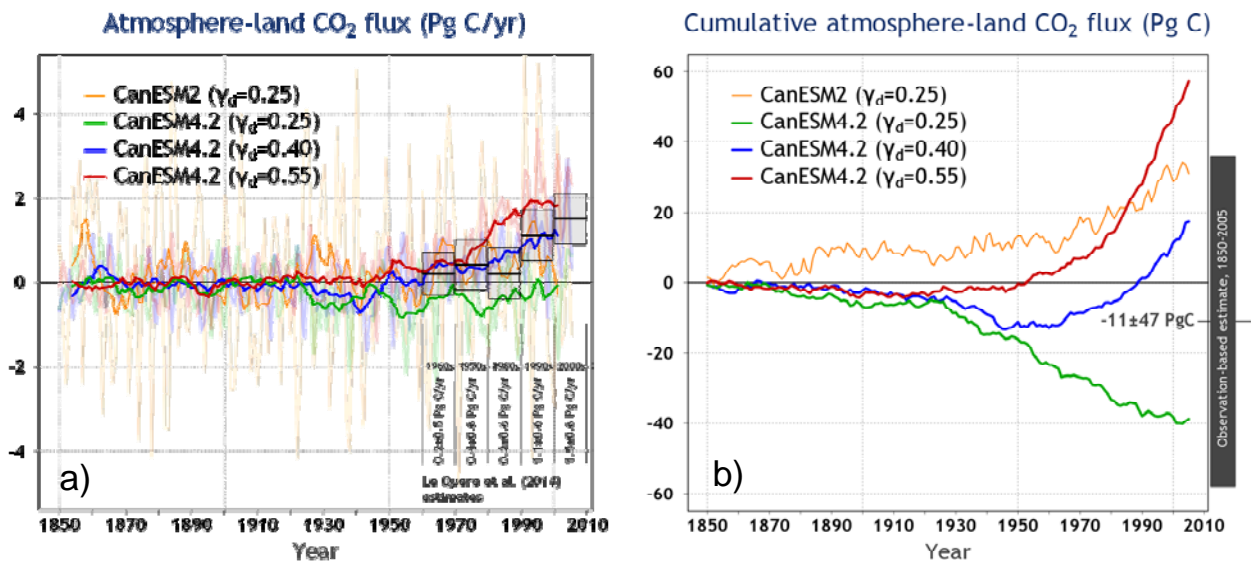


1039

1040

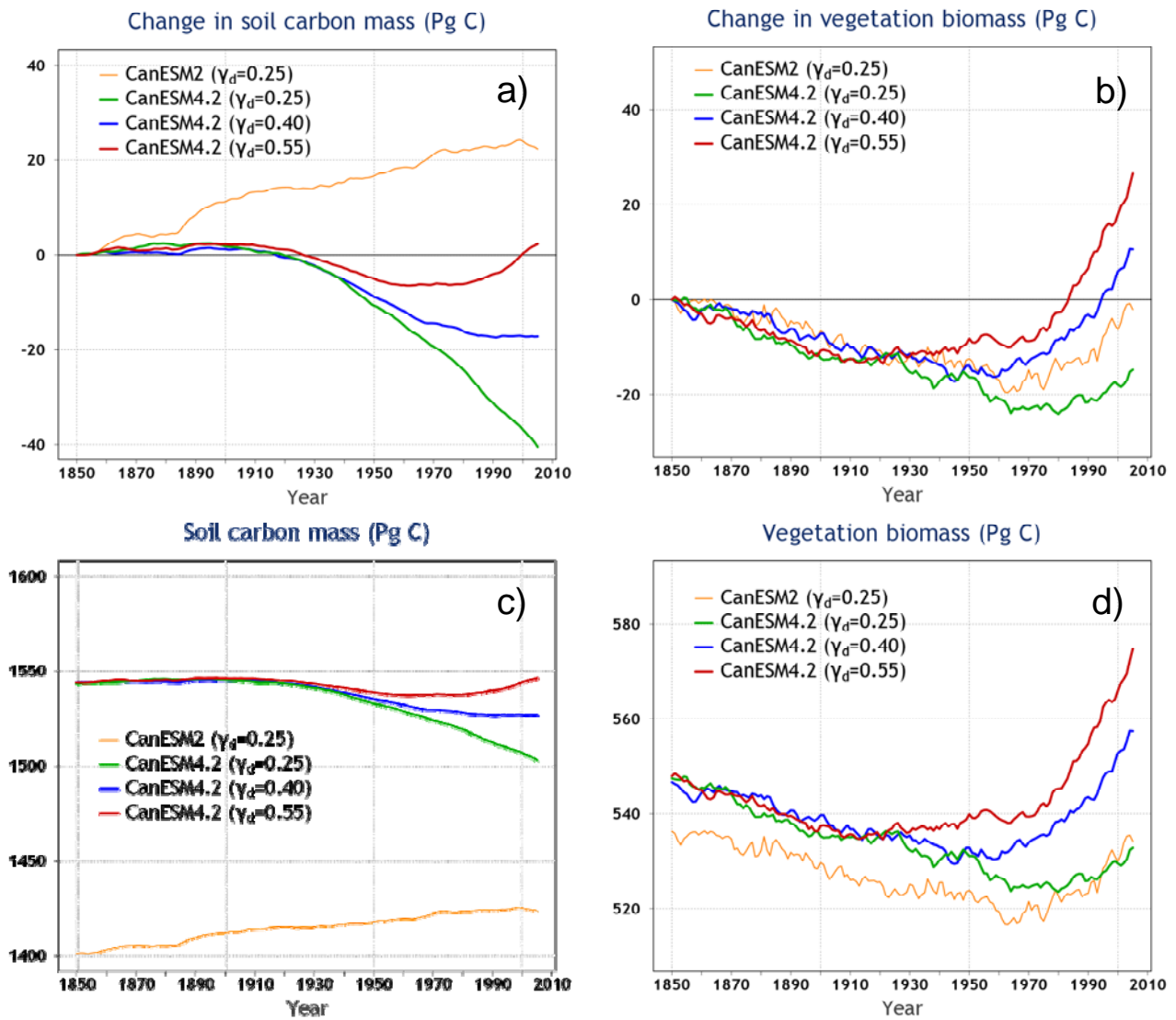
1041 Figure 3: CanESM2 (panel a) and CanESM4.2 (panel b, $\gamma_d=0.40$) precipitation anomalies
1042 compared to the observation-based estimates from CPC Merged Analysis of Precipitation
1043 (CMAP) based on Xie and Arkin (1997) averaged over the 1979–1998 period.
1044

1045
1046
1047
1048
1049



1050
1051
1052
1053
1054
1055
1056
1057
1058
1059

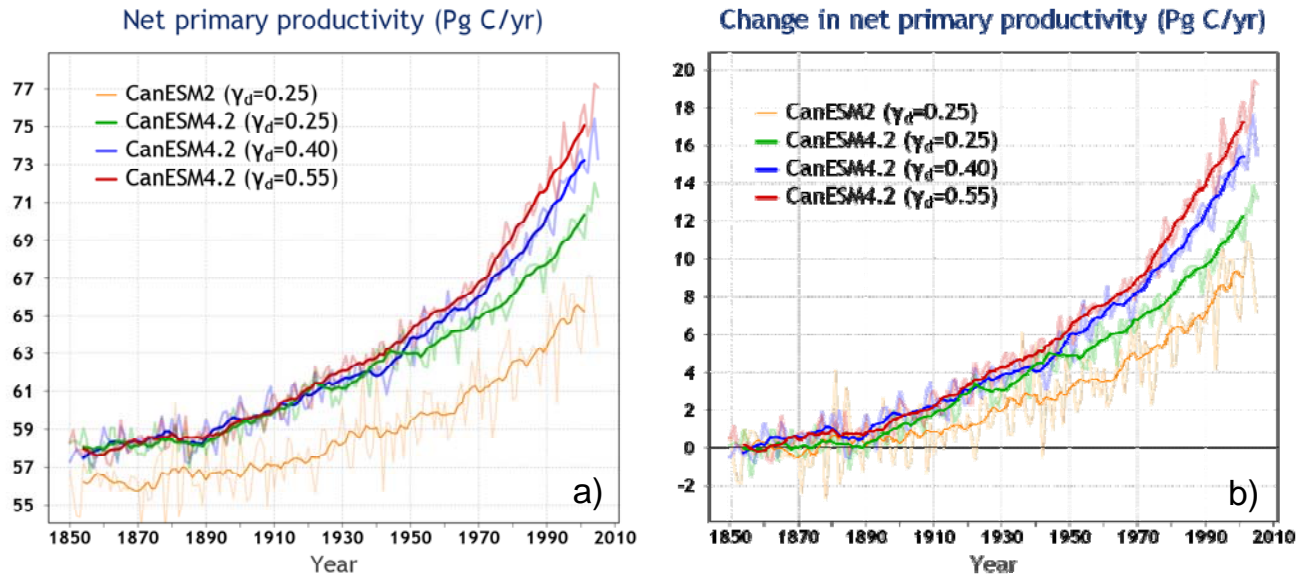
Figure 4: Atmosphere-land CO₂ flux (F_L) (panel a) and its cumulative values \tilde{F}_L (panel b) from CanESM2 and the three CanESM4.2 historical 1850-2005 simulations for different strengths of the terrestrial CO₂ fertilization effect. In panel (a) the observation-based estimates of F_L and their uncertainty, show via boxes, for the decades of 1960, 1970, 1980, 1990 and 2000 are reproduced from Le Quéré et al. (2015). The bold lines in panel (a) are the 10-year moving averages of the annual F_L values which are shown in light colours. The results from CanESM2 and CanESM4.2 are the average of the two ensemble members.



1062 Figure 5: Change in and absolute values of global soil carbon and vegetation biomass amounts
 1063 from CanESM2 and the three CanESM4.2 historical 1850-2005 simulations with different
 1064 strengths of the terrestrial CO₂ fertilization effect. The results shown in all panels are the average
 1065 of the two ensemble members.

1069

1070



1071

1072 Figure 6: Absolute values of (panel a), and change in (panel b), net primary productivity (NPP)
1073 from CanESM2 and the three CanESM4.2 historical 1850-2005 simulations with different
1074 strengths of the terrestrial CO₂ fertilization effect. The thin lines show the ensemble-mean based
1075 on results from the two ensemble members and the bold lines are their 10-year moving averages.

1076

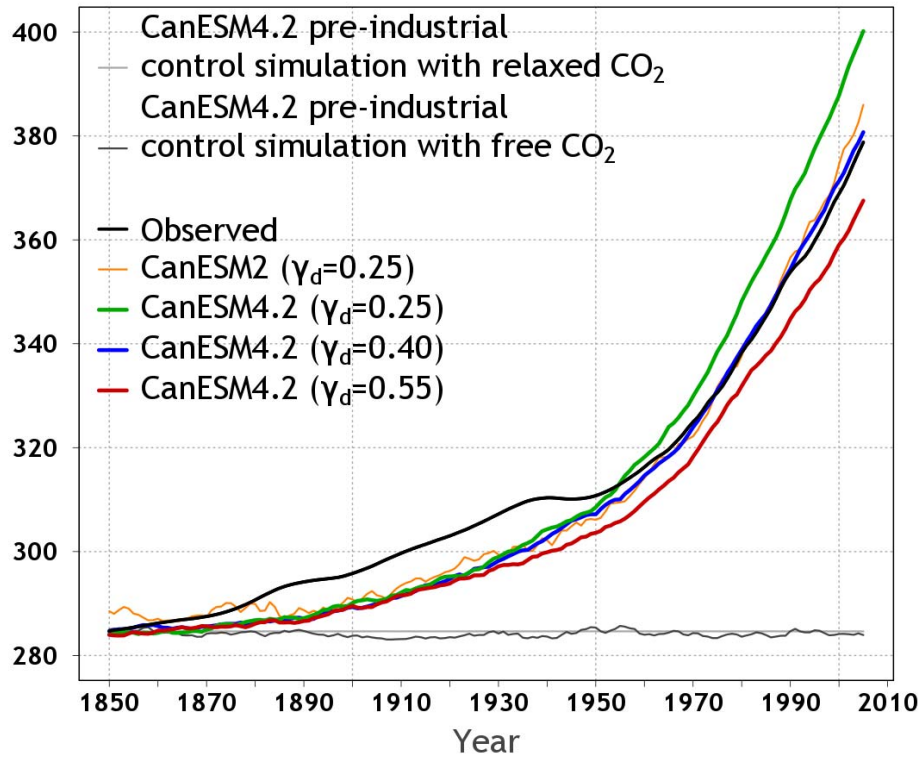
1077

1078

1079

1080

Globally-averaged surface CO₂ concentration (ppm)

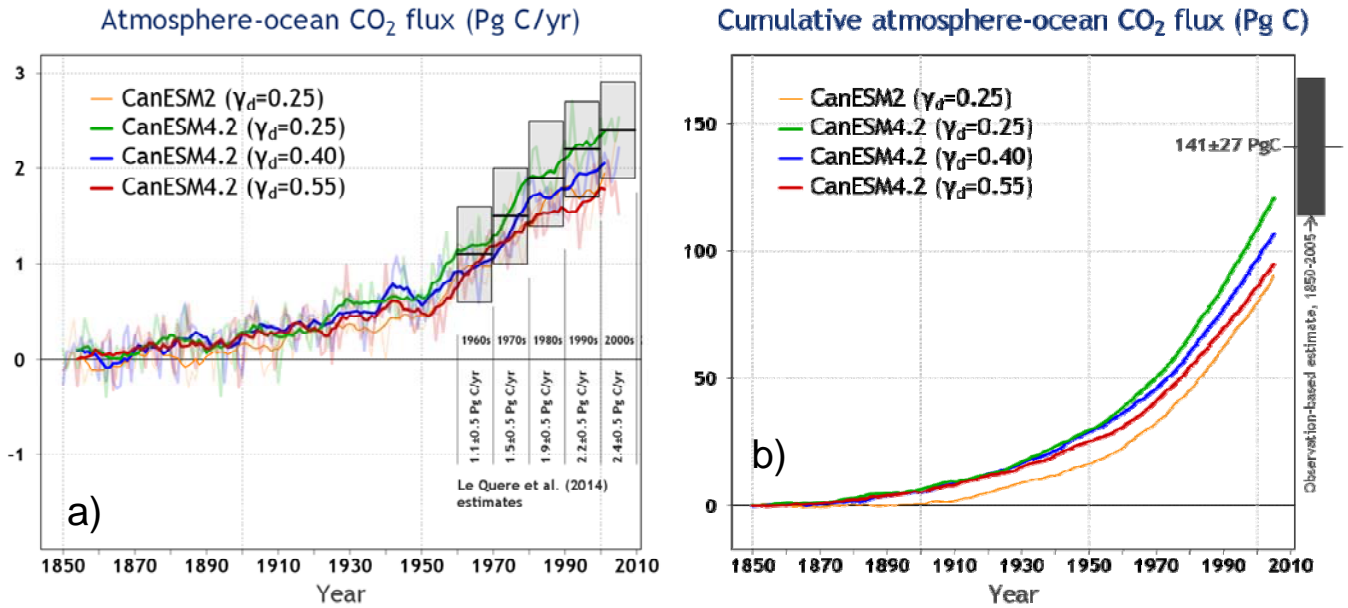


1081

1082 Figure 7: Simulated globally-averaged surface atmospheric CO₂ concentration from CanESM2
1083 and the three CanESM4.2 historical 1850-2005 simulations with different strengths of the
1084 terrestrial CO₂ fertilization effect. The observation-based concentration is shown in black. Also
1085 shown is the CO₂ concentration of 284.6 ppm used in CanESM4.2's pre-industrial simulation in
1086 the relaxed-CO₂ configuration and the simulated concentration from the pre-industrial
1087 CanESM4.2 simulation with interactively determined CO₂.

1088

1089
1090
1091



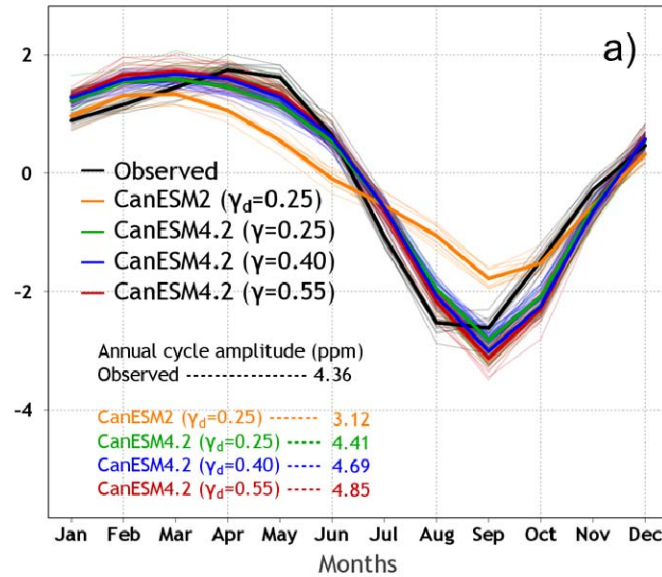
1092

1093 Figure 8: Atmosphere-ocean CO₂ flux (F_O) (panel a) and its cumulative values \tilde{F}_O (panel b) from
1094 CanESM2 and the three CanESM4.2 historical 1850-2005 simulations for three different
1095 strengths of the terrestrial CO₂ fertilization effect. In panel (a) the observation-based estimates of
1096 F_O and their uncertainty, show via boxes, for the decades of 1960, 1970, 1980, 1990 and 2000 are
1097 reproduced from Le Quéré et al. (2015). The bold lines in panel (a) are the 10-year moving
1098 averages of the annual F_L values which are shown in light colours. The results from CanESM2
1099 and CanESM4.2 are the average of the two ensemble members.

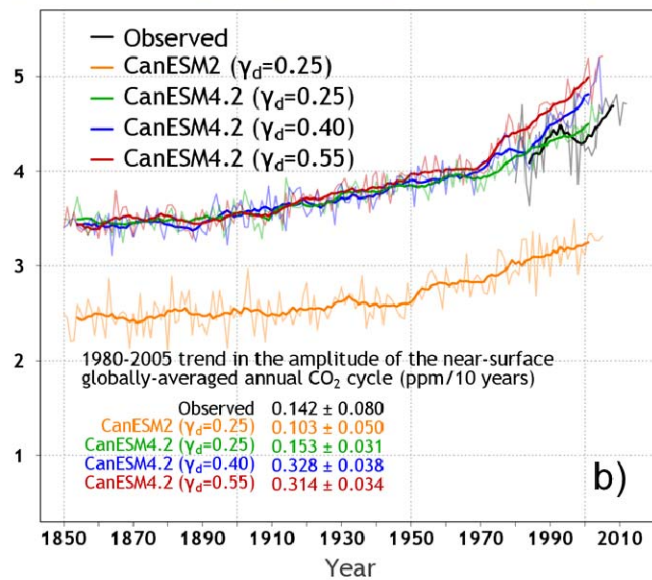
1100

1101

Monthly CO₂ cycle trend-adjusted anomalies (ppm) 1991-2000



Amplitude of the globally-averaged annual CO₂ cycle (ppm)



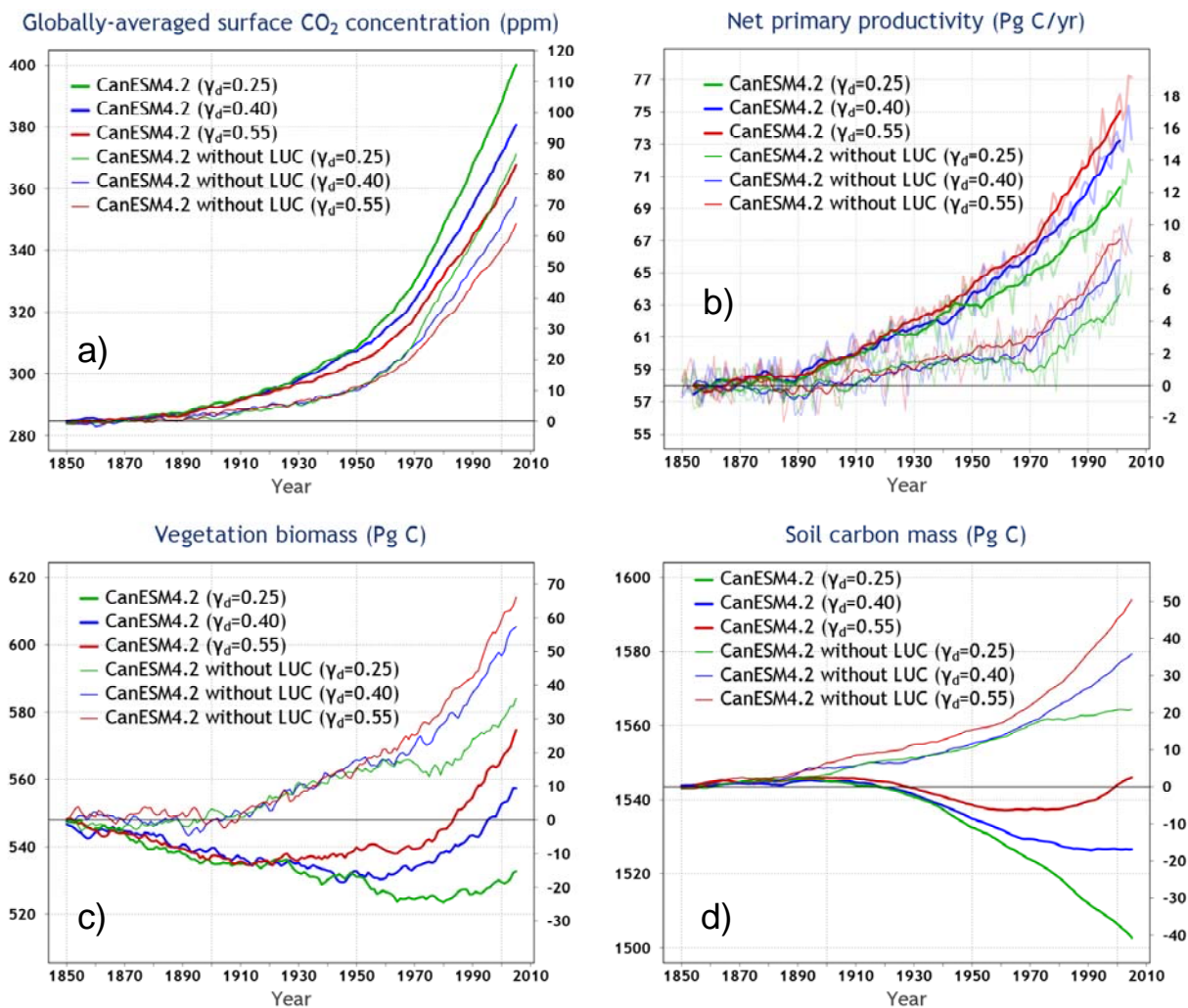
1102

1103 Figure 9: The annual cycle of trend-adjusted globally-averaged near-surface monthly [CO₂]
 1104 anomalies from CanESM2, the versions of CanESM4.2 for three different strengths of the CO₂
 1105 fertilization effect and observation-based estimates for the 1991-2000 period (panel a). Panel (b)
 1106 shows the time series of the amplitude of the annual cycle of the trend adjusted globally-averaged
 1107 near-surface monthly [CO₂] anomalies for corresponding model and observation-based estimates.
 1108 The bold lines are 10-year moving averages and the thin lines for model results are the average of
 1109 results from two ensemble members.

1110

1111

1112



1113

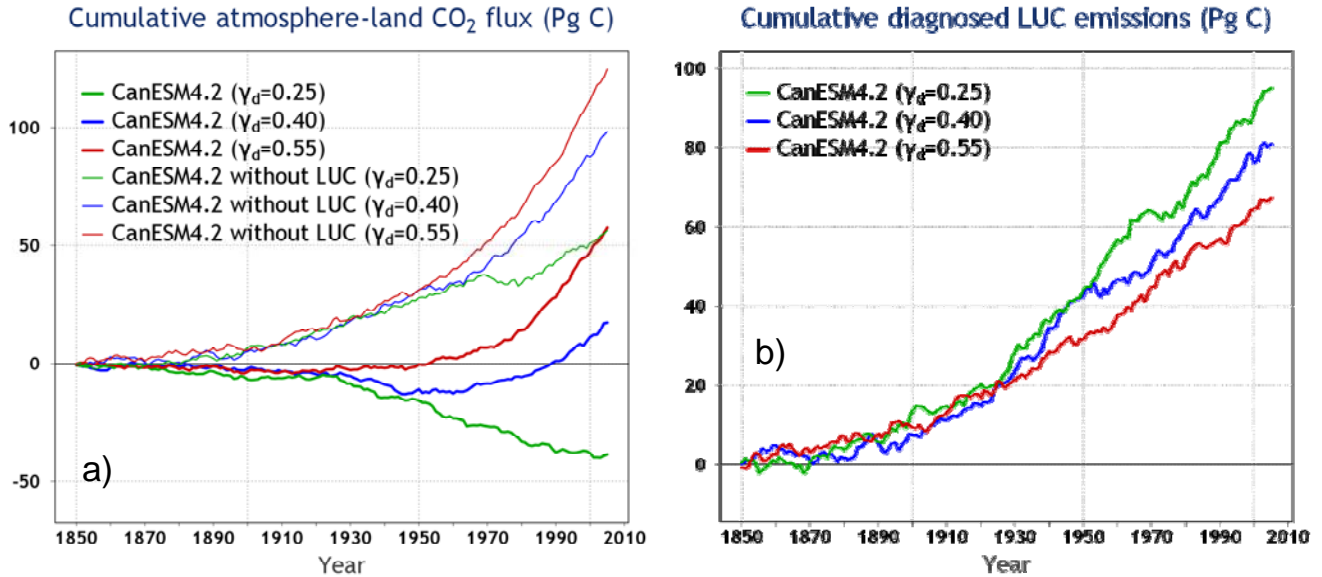
1114 Figure 10: Comparison of CanESM4.2 simulations with and without implementation of
1115 anthropogenic land use change over the historical period for three different strengths of the
1116 terrestrial CO₂ fertilization effect: a) Globally-averaged annual surface atmospheric CO₂
1117 concentration, b) net primary productivity, c) global vegetation biomass, and c) global soil carbon
1118 mass. All lines are the average of results from two ensemble members. Additionally, in panel (b)
1119 the bold lines are the 10-year moving averages.

1120

1121

1122

1123



1124

1125

1126 Figure 11: Comparison of simulated cumulative atmosphere-land CO₂ flux from CanESM4.2
1127 simulations with and without implementation of anthropogenic land use change over the historical
1128 period for three different strengths of the terrestrial CO₂ fertilization (panel a). Panel (b) shows
1129 the cumulative diagnosed LUC emissions calculated using equation (10) as the difference
1130 between cumulative atmosphere-land CO₂ flux from simulations with and without LUC shown in
1131 panel (a). All lines are the average of results from two ensemble members.

1132

1133

1134